Kondo-Majorana coupling in Double Quantum Dots.

by

Jesús David Cifuentes Pardo

Advisor: Luis Gregorio Dias da Silva

MASTER OF SCIENCE

in

Instituto de Física

(Condensed Matter Physics)

UNIVERSIDADE DE SÃO PAULO

(R. do Matão, 1371 - Butantã, São Paulo)

January 25, 2019

Chapter 1

Abstract

In the last decades the interest in the “search of Majorana fermions” in condensed matter systems [1] has increased due to their potential applications in quantum computing. As recently as 2012, experimental works reporting the detection of such quasiparticles [2, 3]. Later works [4, 5, 6, 7], including a recent paper published by the advisor of this dissertation and collaborators [8], set out to explore the interplay of such Majorana zero-modes with strongly interacting systems such as semiconductor quantum dots, which can be readily integrated in the device. This research project aims to expand this idea using the numerical renormalization group to study the model of a double quantum dot coupled to metallic leads and to a topological superconductor supporting edge Majorana zero modes. This simple model allows the manipulation of the majorana modes bringing possible applications to braiding procedures . In addition, we will study the interplay of Kondo correlations, exchange interactions and Majorana physics.

Chapter 2

Table of Contents

Appendices

Chapter 3

Preliminaries

We will start with a description of transport processes in QDs which will lead us to talk about the Anderson model. Then we will take a look to the Kondo effect and, in particular, to its consequences in quantum dots.

3.1 Transport in Quantum Dots (QDs)

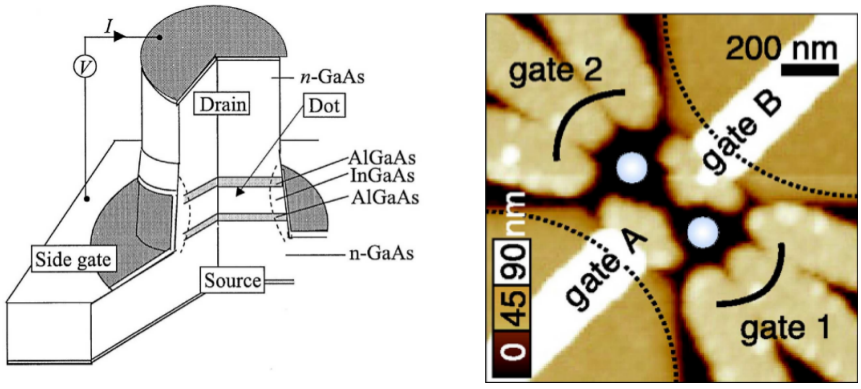

(a) (b)

Figure 3.1: a) Vertical quantum dot. b)Atomic force microscopy picture of two coupled lateral QDs (bright central circles). Gates 1 and 2 act as drain and source voltage. A negative voltage is applied at gates A,B to allow the formation of the droplets inside the free space in the 2D electron gas.
Source: *[9]*

Quantum mechanical effects are visible when the system size is of the order of the de Broglie wavelength [10, (1.1)]

$$\lambda_f = \frac{h}{\sqrt{3 m_{\text{eff}} k_B T}}$$

where m_{eff} is the electron effective mass in the crystal. Since m_{eff} can be much smaller than the free electron mass in some semiconducting materials, size quantization effects can be observed at system of sizes $\sim$ 100nm [11, 2.1]. A 0D quantum system is a device confined in the three

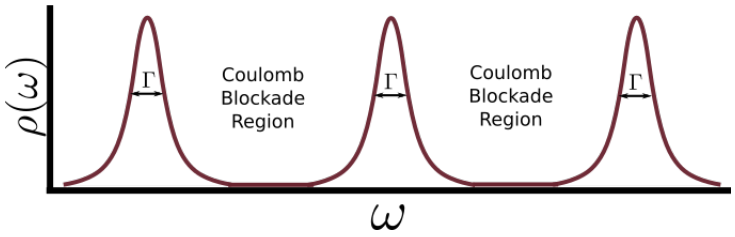

Figure 3.2: Pictorial representation of the Density of States of a QD. The gate potential V_G can be tuned to change the fermi energy of the dot.
Source: *By the author*

spacial dimensions up to this length-scale. This type of devices receive the name of quantum dots (QD).

Nowadays, QDs can be manufactured with several methods, forms and orientations [10]. Note *Methods and forms* According to their orientation with respect to the based 2D-plane two main types of QDs can be distinguished : Vertical (Figure 3.1a) and lateral (Figure 3.1b) QDs.

Both types of quantum dots have 3-main gates. Two of them are the Drain V_D and source V_S gate voltages used to control the current through the QD. The third one is the gate voltage V_G which controls the electron confinement inside the QD by tuning the the energy levels .

Ideally, the energy spectrum of a QD is a discrete set of energy levels resembling the spectrum of an atom. However, when the QD is connected to metallic leads these energy levels hybridized with respect to a hybridization parameter Γ which depends on the voltage connecting the lead with the dots V as

$$\Gamma \propto \pi \|V\|^2 \tag{3.1}$$

in a flat band. A representation of this fact can be found in Figure 3.2. Ideally, $\Gamma \ll \Delta E$ such that the energy levels do not overlap each other. In addition the gate voltage allows us to tune the energy levels of the QD.

It is possible to execute transport measurements through a QD by attaching it to two leads, source and drain (See 3.3a) . Each lead will have a characteristic gate voltage V_S (Left lead) and V_D (Right lead). An electron can pass from the source to the drain if there is an energy level in the middle of the two voltages, just as in 3.3a. If this condition is not satisfied, the dot enters into a coulomb blockade region without electron transport between both leads as can be observed in 3.4b. Inside the coulomb blockade regions the number of electrons is constant. When increasing V_G a single electron enters into the dot each time. Since all of these effects can be controlled by a tuning the gate voltage, the system described is indeed a single electron transistor (SET).

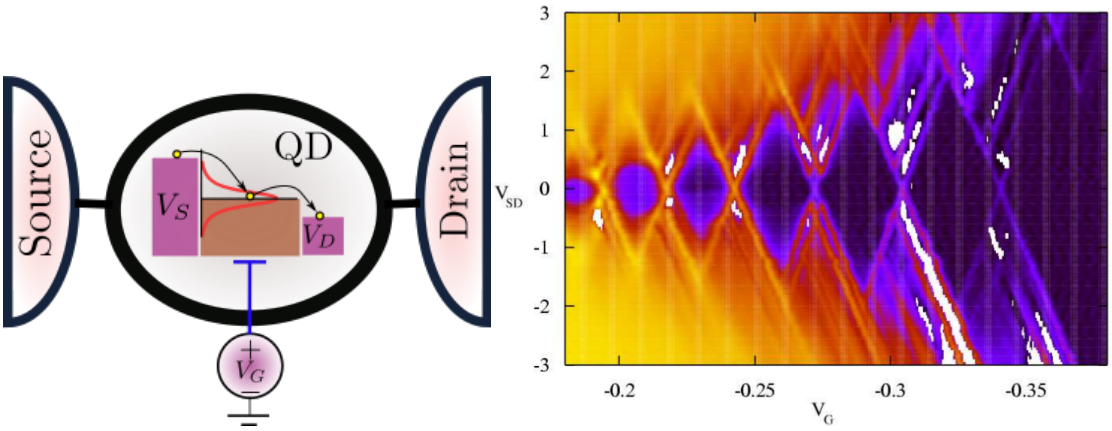

(a) (b)

Figure 3.3: a) Representation of transport through QD. The red curve represents the hybridized energy level. The gate voltage tunes this level. In the case represented, the energy level is in the middle of the drain and source voltages allowing transport between the leads. Charging diagram of a quantum dot. b) Plot of the conductance vs the gate voltage V_G and the source-drain voltage $(V_{SD} = V_S - V_D)$

Source: *a) By the Author , b) [11]*

3.2 The Anderson Model

The key ingredient in the Kondo phenomena is the presence of magnetic impurities whose states are hybridized to conduction electron in the metal. To study this idea the physics Nobel prize winner Philip Anderson created a model that simulated the quantum interaction between the impurity and the conduction band [12]. The Anderson Model can be applied to different problems. In this thesis we are mainly interested in the study of artificially manufacture impurities better known as quantum dots.

Due to the small confinement space inside these dots, the coulomb repulsion is relevant. However, it is usually impossible to provide a complete analytical description of these kind of systems due to the high correlations generated by this factor. Instead, we can obtain an overall description of the transport through the impurity by neglecting this coulomb repulsion. This will allow us to obtain some analytic intuition of the models before adventuring with long-lasting numerical simulations of interacting models. During this thesis, we will consider these two regimes as follows

- **Non-interacting systems:** Coulomb repulsion is not relevant . In this case, spin-$\uparrow$ and spin-$\downarrow$ channels are independent which simplifies many of the procedures. They can be described analytically through the ballistic transport approach.

- **Interacting systems:** The coulomb repulsion is relevant. The repulsion factor will be defined by the factor U which will take a fix value during the entire project. In this case, spin-$\uparrow$ and spin-$\downarrow$ channels are not independent since the coulomb repulsion limits the number of particles inside each dot. We will use the Numerical Renormalization Group to treat this case. The intuition acquired from non-interacting systems will help us to select the input parameters of the algorithm.

With these cases in mind lets consider in general that the system is interacting with a coulomb repulsion factor of U which will be set to 0 if the system is non-interacting .

To build the Anderson model first consider that we have a QD (impurity) coupled to the conduction band of a metallic lead. Using the Hunds rules we know that the energy levels inside the dot should be filled from lower to higher energies with two electrons with different spin at each state. Each pair of electrons will interact magnetically and electrically. In addition, there is and energy term associated to each electron and a Zeeman splitting factor in case a $\hat{z}$-directed magnetic field B is placed. Considering these interactions we can obtain a very general expression in second quantization for the QD Hamiltonian of the form [11, (3.2)]

$$H_d = \sum_{i\sigma} \varepsilon_{di} d^\dagger_{i\sigma} d_{i\sigma} + \sum_i U_i \hat{n}_{i\uparrow}\hat{n}_{i\downarrow} + \sum_{\sigma\sigma',i\neq j} U_{ij}\hat{n}_{i\sigma}\hat{n}_{j\sigma'} - \mu_B g B \sum_i S^z_i + J\sum_{i\neq j} \mathbf{S}_i \cdot \mathbf{S}_j.$$

Where $\sigma \in \{\uparrow,\downarrow\}$, $d^\dagger_{i\sigma}\,(d_{i\sigma})$ is the dot creation(annihilation) operator,$\hat{n}_{i\sigma} := d^\dagger_{i\sigma} d_{i\sigma}$ is the particle number, $\mathbf{S}_i$ is the spin-vector, ε_{di} is the energy of the i^{th}-level in the dot, U_i is the coulomb repulsion between electrons in the same energy level i, U_{ij} is the coulomb interaction between electrons in different levels (And therefore smaller than U_i), B is an applied magnetic field in the $\hat{z}$-direction and J is the term representing the Zeeman splitting.

At low temperatures, the quantum interactions occur only with the level closest to the Fermi energy. This allows us to make the single-level approximation, neglecting the other energy levels. This assumption reduces the complexity of the dot Hamiltonian to

$$H_d = \sum_\sigma \varepsilon_d d^\dagger_\sigma d_\sigma + U\hat{n}_\uparrow\hat{n}_\downarrow - \mu_B g B S^z. \tag{3.2}$$

Besides to the dot Hamiltonian, we need to consider the energy of the electrons in the lead H_{lead} and the dot-lead interaction H_{int}. We can model the conduction band of the lead as a $2D$ electron gas with the following Bloch Hamiltonian

$$H_{lead} = \sum_{\mathbf{k}\sigma l} \varepsilon_{\mathbf{k}l} c^\dagger_{\mathbf{k}\sigma l} c_{\mathbf{k}\sigma l}. \tag{3.3}$$

where $\mathbf{k}$ represents the possible crystal momentums in the leads, $l \in \{S,D\}$, $c^\dagger_{\mathbf{k}\sigma l}(c_{\mathbf{k}\sigma l})$ creates(annihilates) an electron with momentum $\mathbf{k}$ and spin σ in the lead l, $\varepsilon_{\mathbf{k}l}$ is the energy of the electron in the leads.

The interaction between the dot and the leads is then given by

$$H_{int} = \sum_{\mathbf{k}\sigma l} V_{\mathbf{k}l} c^{\dagger}_{\mathbf{k}\sigma l} d_{\sigma} + V^{*}_{\mathbf{k}l} d^{\dagger}_{\sigma} c_{\mathbf{k}\sigma l}, \tag{3.4}$$

where $V_{\mathbf{k}l}$ is a hopping exchange term between the leads and the QD.
The sum of all of these three interactions is receives the name of Anderson Model.

$$\begin{aligned} H &= H_d + H_{lead} + H_{int} \\ &= \sum_{\sigma} \varepsilon_d d^{\dagger}_{\sigma} d_{\sigma} + U \hat{n}_{\uparrow} \hat{n}_{\downarrow} - \mu_B g B S^z + \sum_{\mathbf{k}\sigma l} \varepsilon_{\mathbf{k}l} c^{\dagger}_{\mathbf{k}\sigma l} c_{\mathbf{k}\sigma l} + \sum_{\mathbf{k}\sigma l} V_{\mathbf{k}l} c^{\dagger}_{k\sigma l} d_{\sigma} + V^{*}_{\mathbf{k}l} d^{\dagger}_{\sigma} c_{\mathbf{k}\sigma l}. \end{aligned} \tag{3.5}$$

For this project, we will make two extra changes to the Anderson model. Using the anti-commutation properties of the fermion operators

$$\left\{ d^{\dagger}_{\sigma}, d_{\sigma'} \right\} = \delta_{\sigma\sigma'} \ , \ \left\{ d^{\dagger}_{\sigma}, d^{\dagger}_{\sigma'} \right\} = \{ d_{\sigma}, d_{\sigma'} \} = 0$$

we get

$$\begin{aligned} \left(d^{\dagger}_{\uparrow} d_{\uparrow} + d^{\dagger}_{\downarrow} d_{\downarrow} - 1 \right)^2 &= \sum_{\sigma} \left(d^{\dagger}_{\sigma} d_{\sigma} \right)^2 - 2 \sum_{\sigma} d^{\dagger}_{\sigma} d_{\sigma} + 2 d^{\dagger}_{\uparrow} d_{\uparrow} d^{\dagger}_{\downarrow} d_{\downarrow} - 1 \\ &= 2 d^{\dagger}_{\uparrow} d_{\uparrow} d^{\dagger}_{\downarrow} d_{\downarrow} - \sum_{\sigma} d^{\dagger}_{\sigma} d_{\sigma} - 1. \end{aligned}$$

Replacing this in (3.2) we obtain a nice spin-symmetric form of the dot hamiltonian

$$\left(\varepsilon_d + \frac{U}{2} \right) d^{\dagger}_{\sigma} d_{\sigma} + \frac{U}{2} (d^{\dagger}_{\sigma} d_{\sigma} - 1)^2 - \mu_B g B S^z. \tag{3.6}$$

In addition, it is possible to do a linear transform to the lead opperators

$$\frac{1}{\sqrt{V_S^2 + V_R^2}} \begin{bmatrix} V_S & V_R \\ -V_R & V_S \end{bmatrix} \begin{bmatrix} c_{\mathbf{k}\sigma S} \\ c_{\mathbf{k}\sigma D} \end{bmatrix} = \begin{bmatrix} c_{\mathbf{k}\sigma +} \\ c_{\mathbf{k}\sigma -} \end{bmatrix} \tag{3.7}$$

After the transformation the operator will be decoupled from the dot hamiltonian $c_{\mathbf{k}\sigma -}$. This implies that we can suppose that the **dot is coupled wit just one lead**. During the rest of the thesis we will maintain this convention.

3.3 The Kondo Effect

The Kondo effect is one of the biggest condensed matter problems in the 20th century. It counted with the participation of an uncountable number of experimentalist that contributed to this problem. In addition, had an strong theoretical activies led by the physicists Jacques Friedel, Jun Kondo and the two nobel prizes Philip Anderson and Kenneth Wilson [13].

The history of the Kondo effect began in the early 1930s. By that time it was known that the resistivity of a metal is regulated by different scattering interactions against lattice phonon vibrations $\rho_{phonon} \sim T^5$, other electrons $\sim T^2$ and static impurities which is temperature independent. The form of these contribution clearly implies that the resistivity should decay uniformly with a decreasing temperature. Nevertheless, those years groundbreaking experiments revealed the observation of a resistance minimum in some metals at temperatures lower than $10K$ (See 3.4a).

This phenomenon intrigued the scientific community for the following decades until the year 1964 when the physicist Jun Kondo gave the first convincing solution to this puzzle. Kondo attributed the phenomenon to the scattering of the electrons due to the spin-interaction with a small concentration of magnetic impurities in the metal. To describe it he proposed the following interaction Hamiltonian

$$H_K = 2J\hat{\mathbf{S}} \cdot \hat{\mathbf{s}} \tag{3.8}$$

$$= J(2S_z s_z + S_+ s_- + S_- s_+) \tag{3.9}$$

with $S_\pm = S_x \pm iS_y$. The hamiltonian H_K which is better known as the Kondo s-d model describes the spin interaction between the spin of the impurity $\hat{\mathbf{S}}$ and the spin of the particles in the metal $\hat{\mathbf{s}}$.

Kondo took H_K as a perturbation of the electron gas inside metallic lead, with J the perturbation parameter. While the first order led to no important contribution, Kondo was able to obtain on second order perturbation theory a logarithmic correction on the temperature in the resistivity of the form

$$\rho_{imp} \propto \ln \frac{T_K}{T}, \tag{3.10}$$

where T_K received the name of Kondo temperature. Summing up this term to the other resistivity contributions we obtain the full expression

$$\rho_{metal}(T) = \rho_{imp} + a_e T^2 + b_{Phonon} T^5 + c_m \ln \frac{T_K}{T}. \tag{3.11}$$

Note that when $T < T_K$ the term $\ln \frac{T_K}{T}$ increases, so that it will eventually compensate the decaying resistivity which finally explained the resistance minimum.

Although Kondo's explanation was initially very successful it also presented a troublesome outcome. The logarithmic term introduced by Kondo diverges when the temperature approximates to 0, hence proving to be inefficient at temperatures well bellow T_K. Going to the following orders in perturbation theory also led to divergent resistivities which led the following physicist to explore alternative non-pertubative approaches to the Kondo effect.

On the other hand, Anderson had already created by that his famous impurity model. One of his main contributions was the inclusion of the Hubbard term to represent the coulomb interaction inside the dot, which proofed to be fundamental to understand the Kondo effect. Years

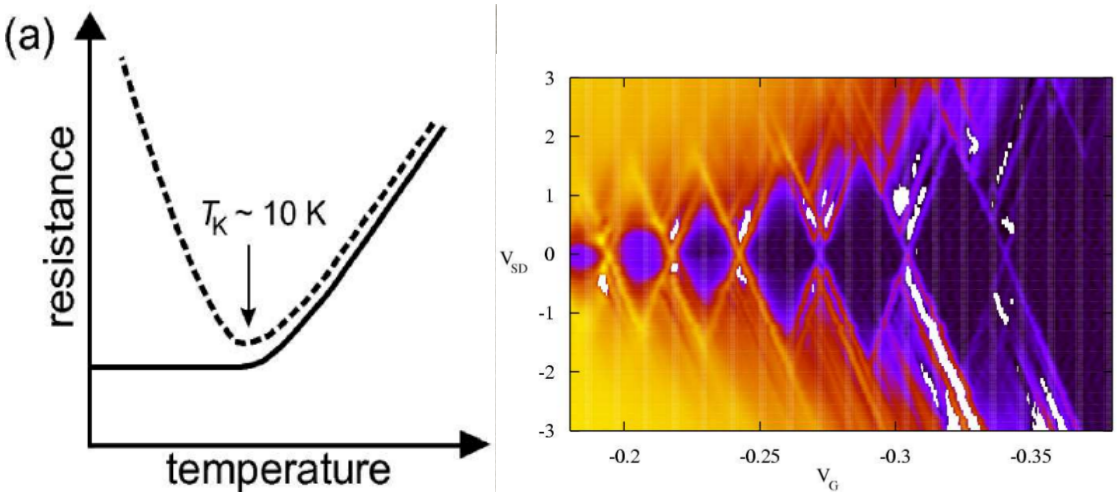

(a) (b)

Figure 3.4: a) Representation of transport through QD. The red curve represents the hybridized energy level. The gate voltage tunes this level. In the case represented, the energy level is in the middle of the drain and source voltages allowing transport between the leads. Charging diagram of a quantum dot. b) Plot of the conductance vs the gate voltage V_G and the source-drain voltage $(V_{SD} = V_S - V_D)$

Source: *a) [14] , b) [11]*

later Kenneth Wilson was able to effectively diagonalize the Anderson model using a numerical method that combines ideas from scalability and the renormalization group. This allowed him to include low-energy contributions which are the ones responsible for the strong correlations in the Kondo effect.

Wilson's numerical renormalization group

The resistivity of materials is known to decay linearly with

In low temperature metals the resistivity decays uniformly with the temperature due to the absence of scattering electrons at lower energies. However, in the early 30s the physicist where intrigued by the observation of a resistance minimum in some metals at temperatures near to $10K$ [11]. The effect was studied by the material physicist Kondo who attributed this phenomenon to a small concentration of magnetic impurities in the metal [13]. Kondo explained that the conducting electrons in the metal scattered with the electrons in the impurity due to the spin interaction.

The resistivity of a metal is normally regulated by different scattering parameters including lattice vibrations $\rho_{phonon} \sim T^5$

Using perturbation theory is possible to explain how this spin flip produces a temperature dependent effect which introduces an additional logarithmic term to the resistivity of the form

$$\rho_{Kondo}(T) \propto \ln\left(\frac{T_{kondo}}{T}\right), \tag{3.12}$$

which occurs due to the spin-flip between the particles in the impurity and in the reservoir. The entire resistivity including and

We can seen that under the scale of temperature defined by T_k the Kondo effect dominates over all other interactions. However, there is a fundamental problem in the Kondo model. For temperatures much smaller than T_K the resistivity diverges. This problem is solved by applying a re-normalization group approach to treat the strong correlations appearing at low temperatures. In the Kondo problem a logarithmic discretization is used. The numerical procedure receives the name of Numerical renormalization Group (NRG).

3.3.1 Kondo Effect in QDs

The problem of magnetic impurities in metals can be treated using the Anderson model in a similar form as the transport in quantum dots. Hence, it is not a surprise that Kondo Effect could also occur in QDs. When an odd number of electrons is in the QD the last level bellow the Fermi energy is half-occupied and hence the dot is magnetized. The unlocalized electrons in the reservoirs then interact with this localized electron . Spin-exchange can occur as in the case of magnetic impurities in metals. At low temperatures, this magnetic interaction gives rise to strong quantum correlations that favor the formation of a singlet state between the localized electron and the electrons in the leads. As a result, the zero-bias density of states is increased producing a zero-bias conductance peak.

Note that the physical implications of the Kondo effect between the case of magnetic impurities in metals and transport through QD are different. The reason for this is difference in the dimension in both processes . While the scattering at 3D systems against magnetic impurities should produce a drop in the conductivity at low temperatures, the scattering in 0D systems enhances the conductivity of the QD due to the few scattering directions. This implies that the Kondo Effect in QDs acts in the opposite way as in the impurity case.

Chapter 4

Theory and Methods

4.1 Ballistic transport

The Green function G of a Hamiltonian H is the operator that satisfies the homogenous equation

$$\left(i\hbar\frac{\partial}{\partial t} - H\right) G\left(t-t'\right) = \delta(t-t'). \tag{4.1}$$

This type of differential equations are solved taking the Fourier transform

$$G_H(\omega) = \int_{-\infty}^{\infty} G(t-t')e^{i\omega(t-t')/\hbar}\delta(t-t') \tag{4.2}$$

In this new space the solution of the equation is

$$(\omega + is - H)G_\omega(\omega) = I.$$

The term $+is$ in the previous hamiltonian is part of a mathematical trick quite common in this theory. During the whole procedure, the Green function acts on the complex field. But when we need to obtain a physical interpretation we will take the limit $s \to 0$ to obtain the result for real energies. The next step is to decompose $G_H(\omega)$ in the eigenbase of the Hamiltonian $\{|\alpha\rangle\}$ by

$$G_{\alpha,\alpha'}(\omega) = \langle\alpha|G_H(\omega)|\alpha'\rangle = \frac{\delta_{\alpha\alpha'}}{\omega - is - \varepsilon_\alpha} = \frac{\delta_{\alpha\alpha'}(\omega + is - \varepsilon_\alpha)}{(\omega-\varepsilon_\alpha)^2 + s^2}. \tag{4.3}$$

From the famous formula

$$\lim_{s\to 0}\frac{s}{(\omega-\varepsilon_\alpha)^2+s^2} = \pi\delta(\omega-\varepsilon_\alpha) \tag{4.4}$$

we obtain

$$Im[G_{\alpha,\alpha'}(\omega)] = \pi\delta(\omega-\varepsilon_\alpha)\delta_{\alpha,\alpha'}. \tag{4.5}$$

Note that the sum of $Im[G_{\alpha,\alpha}(\omega)]$ over all the eigenstates of H is simply the π times the Density of States:

$$\rho(\omega) = -\frac{1}{\pi} Im\left[G_{\alpha,\alpha}(\omega)^\dagger\right]. \tag{4.6}$$

An extended definition of the Green function can be given in terms of fermionic operators in second quantization. The time-green function for two fermionic operators A and B is

$$G_{A,B}(t-t') = \mathscr{T}[\{A(t),B(t')\}]. \tag{4.7}$$

Here, causality is important, which is the reason why we use the time-order operator $\mathscr{T}$. Again, it is possible to define the green-functions in the energy space applying a Fourier transform. The evolution of these Green functions will be determined by the Schrodinger equation. At the end, the result will be

The equation above receives the name of transport equation. This will be our leading method to compute the green functions of the system. In addition we can define the Density of States associated to an operator A to be

$$\rho_{A,A^\dagger} = -\frac{1}{\pi} Im\left[G_{A,A^\dagger}(\omega)\right]. \tag{4.8}$$

This density of states contains important physical information related to operator A. In our case, operator $A^\dagger$ will be related to the creation operator of a quantum dot $d^\dagger$. Our mean purpose will be to compute the density of states of a quantum dot $\rho_{d,d^\dagger}$. This that allows us to obtain other transport

4.1.1 Using graph theory to solve the transport equations

Solving the transport equations involves dealing with a set of linear equations where all the possible variables including ω , and the Hamiltonian parameters are assumed to be constant. This can be done by Gauss-Jordan elimination, noting that after each elimination process we need to carry on the account in terms of these variables. The solution will be a polynomial fraction with the variable given by these parameters. When the number of operators in the Hamiltonian increases the number of terms in the polynomial grows-up exponentially. This reveals the importance of exploring new methods that could simplify the solution.

The method presented here uses graph theory algorithms that provide a shortcut to Gauss-Jordan elimination [15]. To probe this method we solve here the transport equations for a non-interacting $(U = 0)$ DQD connected to one lead. According to the Anderson model the Hamiltonian for this system looks like

$$H = t_{dots} d_1^\dagger d_2 + t_{dots}^* d_2^\dagger d_1 + \sum_{i=1}^{2} \varepsilon_{di} d_i^\dagger d_i + \sum_k \left(V_i d_i^\dagger c_{\mathbf{k}} + V_i^* c_{\mathbf{k}}^\dagger d_i\right) + \varepsilon_{\mathbf{k}} c_{\mathbf{k}}^\dagger c_{\mathbf{k}}. \tag{4.9}$$

Since the system is non-interacting we ignore the spin-degeneracy of this Hamiltonian. The only new parameter here is the term t_{dots}, which represents the tunneling between both quantum dots. Using equation (**??**) with $B = d_1^\dagger$ and A shifting among other operators we compute the

following transport equations

$$(\omega-\varepsilon_1)\,G_{d_1,d_1^\dagger}(\omega)=1+t_{dots}G_{d_2,d_1^\dagger}(\omega)+V_1^*\sum_{\mathbf{k}}G_{c_\mathbf{k},d_1^\dagger}(\omega) \tag{4.10}$$

$$(\omega-\varepsilon_\mathbf{k})\,G_{c_\mathbf{k},d_1^\dagger}(\omega)=V_1G_{d_1,d_1^\dagger}(\omega)+V_2G_{d_2,d_1^\dagger}(\omega) \tag{4.11}$$

$$(\omega-\varepsilon_2)\,G_{d_2,d_1^\dagger}(\omega)=t_{dots}G_{d_1,d_1^\dagger}(\omega)+V_2^*\sum_{\mathbf{k}}G_{c_\mathbf{k},d_1^\dagger}(\omega) \tag{4.12}$$

This system is already closed which means that we don't need any other equation to find the solution. The matrix form takes the form

$$\begin{bmatrix}\omega-\varepsilon_2 & -V_2 & -t_{dots}\\ -V_2^* & \omega-\varepsilon_k & -V_1\\ -t_{dots}^* & -V_1^* & \omega-\varepsilon_1\end{bmatrix}\begin{bmatrix}G_{c_\mathbf{k},d_1^\dagger}(\omega)\\ G_{d_2,d_1^\dagger}(\omega)\\ G_{d_1,d_1^\dagger}(\omega)\end{bmatrix}=\begin{bmatrix}0\\0\\1\end{bmatrix} \tag{4.13}$$

By convenience we changed the order of the rows in the matrix and we removed the sum over k ($\sum_k$) to simplify the terms in the matrix. We will intert these terms back in the equations at the end of the procedure.

Although this matrix is not Laplacian, the procedure in [15] can still be applied with the downside of loosing part of the speed-up of the algorithm. We still preserve some of the advantages using graphs, such as the possibility of taking minimal cuttings and the relation between Gauss-Jordan elimination and random walks [15] . Both advantages simplify the complexity of the solution.

Now, our objective is to compute the green function $G_{d_{1\downarrow},d_{1\downarrow}^\dagger}(\omega)$. For this we take the graph $\mathscr{G}_{d_1d_2}$ associated to the matrix (4.13). See Figure 4.1.a). The vertexes of this graph are the operators in the first site of the of the green functions $(d_{1\downarrow},d_2,c_k.\ d_1^\dagger)$. $d_1^\dagger$ is not included since it only appears in the second sub-index of the green functions. The edges are given by the non-diagonal sites in the matrix. In addition, an energy parameter is assigned to each vertex, according to the corresponding term in the diagonal. These energies can also be thought as the magnitude of edges connecting each vertex with itself. The plot of the energy parameters in this algorithm is quite important, hence we prefer to keep this name to differentiate them from the other couplings.

The algorithm consists in the following. Each step of Gauss-Jordan elimination leads to a new graph with different energies and couplings. The elimination of a row and column is equivalent to pop the corresponding vertex in the graph. For instance, lets eliminate the first row and column of the matrix in (4.13). For it we just need to subtract the rank-1 matrix with the same first row and first column

$$\begin{bmatrix}\omega-\varepsilon_k & -V_2 & -V_1\\ -V_2^* & \omega-\varepsilon_2 & -t_{dots}\\ -V_1^* & -t_{dots}^* & \omega-\varepsilon_1\end{bmatrix}-\begin{bmatrix}\omega-\varepsilon_k & -V_2 & -V_1\\ -V_2^* & \frac{V_2^*V_2}{\omega-\varepsilon_k} & \frac{V_2^*V_1}{\omega-\varepsilon_k}\\ -V_1^* & \frac{V_2V_1^*}{\omega-\varepsilon_k} & \frac{V_1^*V_1}{\omega-\varepsilon_k}\end{bmatrix}=\begin{bmatrix}0 & 0 & 0\\ 0 & \omega-\varepsilon_2-\frac{V_2^*V_2}{\omega-\varepsilon_k} & -t_{dots}-\frac{V_2^*V_1}{\omega-\varepsilon_k}\\ 0 & -t_{dots}^*-\frac{V_2V_1^*}{\omega-\varepsilon_k} & \omega-\varepsilon_1-\frac{V_1^*V_1}{\omega-\varepsilon_k}\end{bmatrix} \tag{4.14}$$

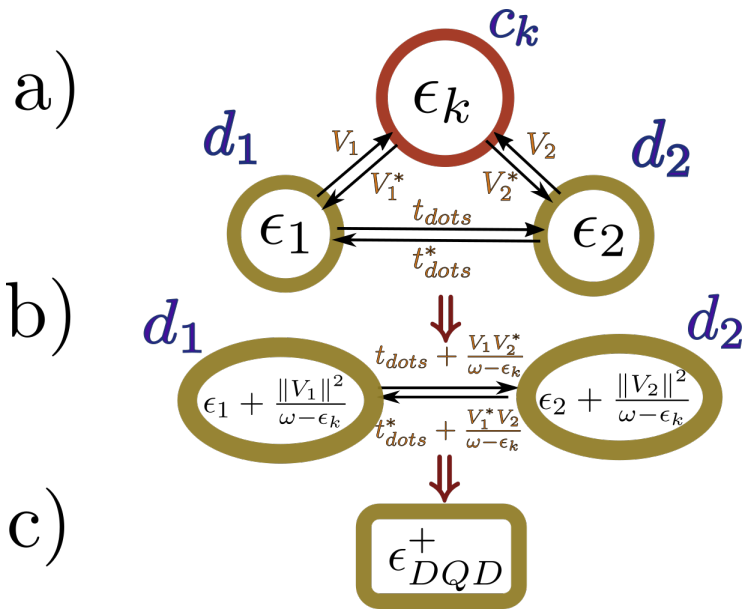

Figure 4.1: Graph representation of Gauss-Jordan elimination a) Graph $\mathscr{G}_{d_1 d_2}$ b) After the elimination of vertex c_k, the energies of dots d_1 and d_2, and the coupling parameter are changed. c) After Gaussian elimination of dot 2 the energy of the remaining dot $\varepsilon_D QD^+$ represents the transport information through d_1 of the entire DQD.

Source: *By the author.*

The graph associated to this matrix can be observed in Figure 4.1.b) where operator c_k has been popped out of the graph. It is possible to associate the correction to the the energies and couplings to the possible walks passing through the vertex c_k. For instance d_1's energy ε_1 receives an extra-term $\frac{V_1^* V_1}{\omega - \varepsilon_k}$ representing an additional walk from d_1 to d_1 passing through c_k. The same logic can be applied to the other terms coupling terms. The correction to t_dots is $\frac{V_1^* V_2}{\omega - \varepsilon_k}$ which corresponds to a path from d_1 to d_2 passing through the popped vertex c_k. Note that this term includes the multiplication both couplings with the vertex divided by the difference of ω with the energy of the vertex. This correspondence between the energy correction and eliminated paths through the graph makes the "popping" process an straightforward task.

We now proceed to pop vertex d_2 which leaves just a single vertex as shown in Figure 4.1.c). The energy of it can be readily computed with the previous path elimination idea which gives

$$\varepsilon^+_{DQD} = \varepsilon_1 + \sum_{\mathbf{k}} \frac{V_1 V_1^*}{\omega - \varepsilon_{\mathbf{k}}} + \frac{\left\| t_{dots} + \sum_{\mathbf{k}} \frac{V_1 V_2^*}{\omega - \varepsilon_{\mathbf{k}}} \right\|^2}{\omega - \varepsilon_2 - \sum_{\mathbf{k}} \frac{V_2 V_2^*}{\omega - \varepsilon_{\mathbf{k}}}}, \tag{4.15}$$

where we selectively included the $\sum_k$-terms in the places where k appeared.

As a result of Gauss-Jordan elimination the linear equation in 4.13 has evolved into the trivial form

$$\begin{bmatrix} 0 & 0 & 0 \\ 0 & 0 & 0 \\ 0 & 0 & \omega - \varepsilon^{+}_{DQD} \end{bmatrix} \begin{bmatrix} G_{c_{\mathbf{k}},d_1^\dagger}(\omega) \\ G_{d_2,d_1^\dagger}(\omega) \\ G_{d_1,d_1^\dagger}(\omega) \end{bmatrix} = \begin{bmatrix} 0 \\ 0 \\ 1 \end{bmatrix}. \tag{4.16}$$

The Green function is then

$$G_{d_1,d_1^\dagger}(\omega) = \frac{1}{\omega - \varepsilon^{+}_{DQD}} = \left[\left(\omega - \varepsilon_1 - \sum_{\mathbf{k}} \frac{V_1 V_1^*}{\omega - \varepsilon_{\mathbf{k}}} \right) - \frac{\left(t_{dots} + \sum_{\mathbf{k}} \frac{V_1 V_2^*}{\omega - \varepsilon_{\mathbf{k}}} \right) \left(t_{dots} + \sum_{\mathbf{k}} \frac{V_1 V_2^*}{\omega - \varepsilon_{\mathbf{k}}} \right)^*}{\omega - \varepsilon_2 - \sum_{\mathbf{k}} \frac{V_2 V_2^*}{\omega - \varepsilon_{\mathbf{k}}}} \right]^{-1}. \tag{4.17}$$

This Green function will be very important in the following chapters where we will compare its behavior with the green function of a Majorana mode.

4.1.2 Graph Algorithm

In this part we summarize the steps of the graph algorithm in order to apply them later to more complicated systems:

1. Computing the transport equations with the second term fixed in the creation operator of $d^\dagger$.
2. Writing the graph associated to the transport system. The vertexes are the operators in the first site of the of the green functions. Energies and couplings are associated to the vertex and edge numbers of the graphs respectively.
3. Popping the vertexes of the graph. Each vertex popping involves the following steps.
   (a) Computing the extra-terms in the energies and couplings based on the walks passing through the popped vertex.
   (b) Eliminating this vertex from the graph.
   (c) Iterating till there is only the vertex d.
4. The energy in the remaining vertex d is $\varepsilon_d = \frac{1}{\omega - G_{d,d^\dagger}(\omega)}$.

This algorithm will be our main method to find the green function and therefore the density of states of any interacting system.

4.1.3 Ballistic transport in a double quantum dot

In this subsection we describe the remaining steps to extract the density of states of the double quantum dot from the Green function 4.17. We will plot the results and observe the evolution of the DOS while tuning the parameters of the model.

First note that equation (4.17) depends on the term $\sum_k \frac{V_i^* V_j}{\omega - \varepsilon_k}$ which describes the broadening of the DOS when the QD enters in contact with the lead. This broadening is usually named $\Gamma_i = V_i^* V_i$ (Or Δ depending on the text book). In general V_i is a function of $\mathbf{k}$. However, in the limit of flat-band we can assume that V_i is constant. Therefore, it is enough to integrate

$$\sum_k \frac{1}{\omega - \varepsilon_k + is} = \int_{-D}^{D} \frac{d\varepsilon_k}{\omega - \varepsilon_k + is} = -\ln\left(\frac{D - \varepsilon_k + is}{-D - \varepsilon_k + is}\right) \xrightarrow[D\to\infty]{} -i, \tag{4.18}$$

where we assumed that there is a maximum energy cutoff D going to infinity in the wide-band limit. Hence

$$-i\Gamma_i = \sum_k \frac{V_i^* V_i}{\omega - \varepsilon_k}. \tag{4.19}$$

We can replace this in equation (4.17) to obtain the real expression for the green function $G_{d_1, d_1^\dagger}(\omega)$. The terms of the form $V_1 V_2^*$ can be replaced for $\sqrt{\Gamma_1 \Gamma_2}$, supposing there is no additional complex phase.

Now, remember from (4.8) that the DOS ρ depends on the imaginary factor of the Green Function $G_{d_1, d_1^\dagger}(\omega)$. This term depends in the broadening Γ. If $\Gamma = 0$ the density of states will be 0 as well. At any other case, one of the dots should be attached to the lead. Let Γ_1 be the broadening of this dot. We will take Γ_1 as our natural unit for the rest of this thesis. In Figure 4.2 we can observe the evolution of the Density of States under certain processes. Each plot includes an inset showing the model applied to the figure. The coupling in purple indicates the tuning variable. We set $e_1 = e_2 = 0$ so that both dots satisfy PHS. The primary results are the

1. **Coupling QD2. Figure 4.2(a)(b):** At $\Gamma_2 = 0$ the second dot is decoupled, hence the first dot's DOS is the same of a single dot case. The maximum height is achieved at $\rho\pi\Gamma_1 = 1$ and the width of this peak is about Γ_1, just as in Figure Figure 3.2. When the second dot is attached $\Gamma_2 > 0$ the density of states is divided between both dots. At $\Gamma_1 = \Gamma_2$ the DOS at the Fermi energy is equal to $\frac{1}{4\pi\Gamma}$ for both dots.

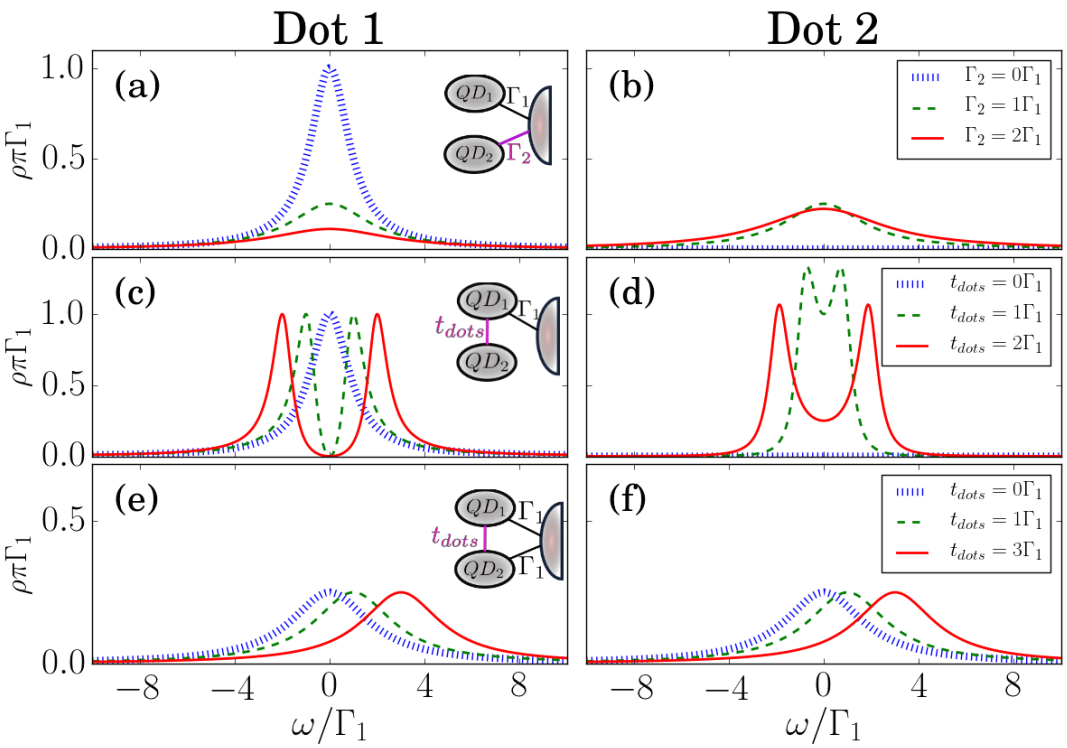

Figure 4.2: Evolution of the density of states at each QD (Left: dot 1, Right: dot 2) at three distinct arrangements of DQD-lead coupling. The inset at the first column depicts the type of coupling. The purple line represents the tuning variable. The energy unit is Γ_1. $e_1 = e_2 = 0$ in all arrangements. (a),(b) The lead is connected to both QDs. Tuning variable: Γ_2. (c)(d) Indirect coupling of the second dot through dot one. Tuning variable: $\_dots$. (e)(f) Triangular coupling. Tuning variable: t_{dots}.

Source: *By the Author*

2. **Indirect Coupling of QD2. Figure 4.2(c)(d):** This is case is interesting. When the second dot is connected indirectly through the first dot, quantum inference splits the central peak in two new states. We will observe later that in the interacting case this procedure can also destroy the Kondo signature.

3. **Breaking Particle Hole Symmetry. Figure 4.2(e)(f):** Suppose we have $\Gamma_2 = \Gamma_1$. The "triangular connections" break Particle Hole Symmetry. The central peak is displaced to the positive part of the spectrum. Contrary to the previous case, this situation will be avoided during this project. This is because this PHS-breaking will prevent the Majorana to tunnel inside the DQD.

4.2 The Numerical Renormalization Group (NRG)

Maybe the most important characteristic of the Kondo effect is that leading contributions to the conductivity are caused by strong correlations with the conduction band appearing at low energy scales. This also explains the divergent logarithmic term in the Kondo resistivity. Indeed, this term predicted by Kondo is a clear signals that the physics of the Kondo effect is different at lower energy scales. The mean problem of pertubative approaches is that they often underestimate these contributions. Instead, a renormalization group approach is able to assign an appropriate effective Hamiltonian to each energy scale based a transformation of the form

$$T[H_N] = H_{N+1}.$$

In the 1970's G.Wilson used this idea to create the famous Numerical Renormalization Group (NRG). His main idea was to perform a logarithmic discretization of the conduction band in the lead as shown in **??**. Taking in account that the mean contributions to the conductance are close to the Fermi energy, we can define a cut-off D where the rest of contributions are not relevant and we use it to rescale the energy interval. As you can observe in the figure, the QD is coupled to all these energy states at the same time. The logarithmic discretization gives more relevance to the low energy scales by assigning a different Hamiltonian coupling to each one of them. To complete this, the NRG code maps the Hamiltonian of the QD-lead system to a chain of the form . A detailed description of in from the logarithmic discretization to the mapping is included in the abstract.

In section 3.3 we observed that the Kondo resistivity had a logarithmic contribution which led to a huge trouble when describing energies bellow the Kondo temperature. This logarithmic term has a especial meaning which is that the lower energy scales are also relevant. Thus, to solve the Kondo problem it was necessary to create a theory that could efficiently integrate the contributions from all energy scales. In the 1970's G.Wilson created a numerical method that mixed ideas from scalability and renormalization group. This method proofed to be the most efficient form to understand the Kondo effect as well as other impurity problems described by the Anderson Model.

Wilson's idea was to discretize the conductance band logarithmically in energy in

In the 1970's G.Wilson created a numerical method to solve the Anderson model . This method receives the name of Numerical Renormalization Group (NRG) [16, 17, 18].

It consists of three basic steps :

1. To perform a numerical discretization of the energy spectrum in logarithmic intervals.
2. To map the discretized model onto a semi-infinity chain Hamiltonian.
3. To diagonalize iteratively the chain hamiltonian .

The final result will be the spectrum of the Hamiltonian. Other important properties of the material such as density of states, conductivity, specific heat, susceptibility can also be computed. On this project we are mainly interested in the Density of States (DOS). The method

used to compute the DOS is the Density Matrix numerical renormalization Group (DM-NRG). A complete description of this algorithm will be given in the followin sections.

For now, we proceed to describe how the NRG is applied to solve the Anderson model in a QD:

Note *I still need to do a long revision to this section. Probably I will send most of the computations to the abstract and leave a summary of NRG and its advantages in the main text.*

Logarithmic Discretization:

We start with an Anderson model hamiltonian such as the one in (3.5) without magnetic field

$$H = \frac{U}{2} + \sum_{\sigma}\left[\left(\varepsilon_d + \frac{U}{2}\right) d_\sigma^\dagger d_\sigma + \frac{U}{2}(d_\sigma^\dagger d_\sigma - 1)^2 + \sum_{\mathbf{k}} \varepsilon_{\mathbf{k}} c_{\mathbf{k}\sigma}^\dagger c_{\mathbf{k}\sigma} + V_{\mathbf{k}} d_\sigma^\dagger c_{\mathbf{k}\sigma} + V_{\mathbf{k}}^* c_{\mathbf{k}\sigma}^\dagger d_\sigma\right]. \tag{4.20}$$

At low-energies we can assume that QD couples only to s-wave states in the leads[18]. This implies that that the Fermi surface is contained in a single, isotropic conduction band extending inside some fixed cutoffs $-D$ and D. Thus, $\varepsilon_{\mathbf{k}}$ only depends on $|\mathbf{k}|$. This makes possible to transform the sum over $\mathbf{k}$ in equation 4.20 into an integral over ε between the energy cutoffs

$$\begin{aligned} H \quad = \sum_\sigma \quad & \left[\left(\varepsilon_d + \frac{U}{2}\right) d_\sigma^\dagger d_\sigma + \frac{U}{2}(d_\sigma^\dagger d_\sigma - 1)^2 + \int_{-D}^{D} \mathrm{d}\varepsilon\ \varepsilon c_{\varepsilon\sigma}^\dagger c_{\varepsilon\sigma} \right. \\ & \left. + \int_{-D}^{D} \sqrt{\rho_\sigma(\varepsilon)}\mathrm{d}\varepsilon\ V_\varepsilon d_\sigma^\dagger c_{\mathbf{k}\sigma} + V_\varepsilon^* c_{\varepsilon\sigma}^\dagger d_\sigma \right]. \end{aligned} \tag{4.21}$$

Here $c_{\varepsilon\sigma}^\dagger$ creates an electron with energy ε and $\rho_\sigma(\varepsilon)$ is the density of states of the system per spin, which appears in the integral due to the change of variable from $\mathbf{k}$ to $\varepsilon \propto |\mathbf{k}|^2$. Finally, we ignore the energy dependence of ρ and V_d and we replace them by their values in the Fermi energy (This approximation has no great relevance which is justified in [18]) and we renormalize the energy band doing the replacements $k = \frac{\varepsilon}{D}$ and $c_{k\sigma} := \sqrt{D} c_{\varepsilon\sigma}$ so that (4.21) becomes

$$\begin{aligned} H \quad &= \quad D\sum_\sigma \left[\frac{1}{D}\left(\varepsilon_d + \frac{U}{2}\right) d_\sigma^\dagger d_\sigma + \frac{U}{2D}(d_\sigma^\dagger d_\sigma - 1)^2 + \int_{-1}^{1} \mathrm{d}k\ k c_{k\sigma}^\dagger c_{k\sigma} \right. \\ &\qquad \left. + \sqrt{\frac{\Gamma}{\pi D}} \int_{-1}^{1} \mathrm{d}k\ d_\sigma^\dagger c_{k\sigma} + c_{k\sigma}^\dagger d_\sigma \right] \qquad (4.22) \\ &= \quad H_d + D\sum_\sigma \left[\int_{-1}^{1} \mathrm{d}k\ k c_{k\sigma}^\dagger c_{k\sigma} + \sqrt{\frac{\Gamma}{\pi D}} \int_{-1}^{1} \mathrm{d}k\ d_\sigma^\dagger c_{k\sigma} + c_{k\sigma}^\dagger d_\sigma \right], \qquad (4.23) \end{aligned}$$

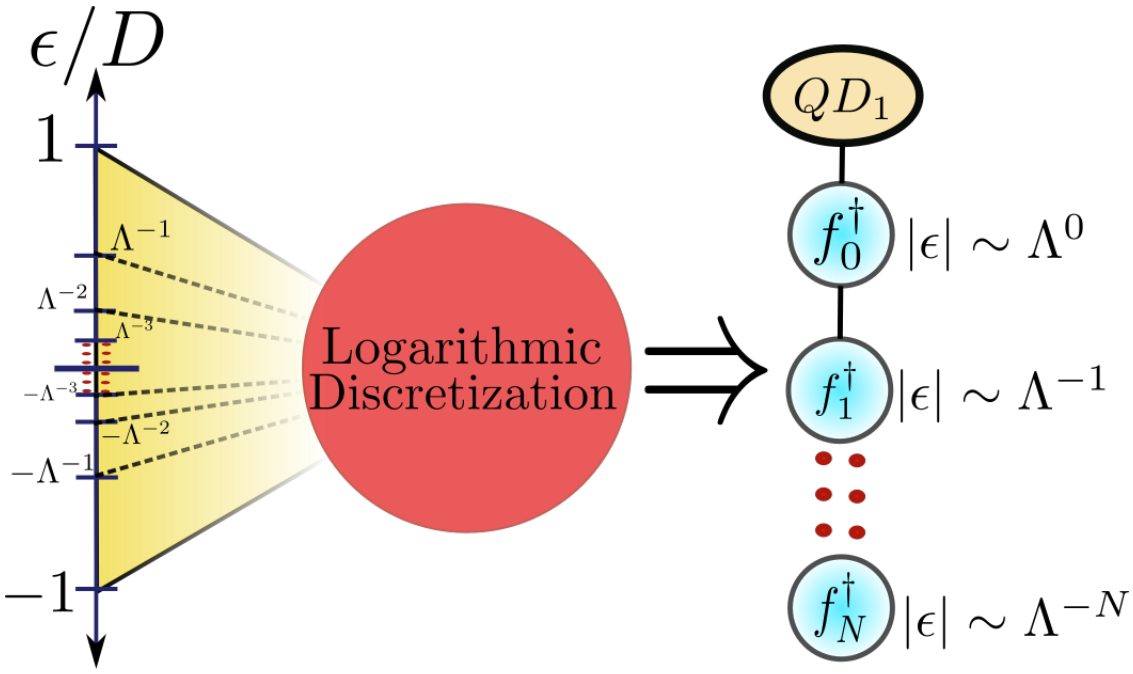

Figure 4.3: . Energy interval discretization. Source: *By the Author*

where $\Gamma = \pi\rho V^2$ is associated to the lever-width [11, (3.5)]. At this point we have our model dependent of three unit-less constants $\frac{\varepsilon_d}{D}$, $\frac{U}{2D}$ and $\frac{\Gamma}{\pi D}$. The logarithmic discretization starts by defining an scaling parameter $\Lambda \geq 1$ in diving the energy domain $[-1,1]$ into an array of intervals of the form $\{[\pm\Lambda^{-(n+1)}, \pm\Lambda^n]\}_{n\in\mathbb{N}}$, as we can observe in Figure 4.3. Note that the width of these intervals is decreasing exponentially by

$$d_n = \Lambda^{-n}\left(1-\Lambda^{-1}\right).$$

Then inside of these energy intervals we can define a set of orthonormal Fourier series of the form

$$\phi_{np}^{\pm}(\varepsilon) = \begin{cases} \frac{1}{\sqrt{d_n}} e^{\pm i\omega_n p\varepsilon} & \varepsilon \in [\pm\Lambda^{-(n+1)}, \pm\Lambda^n] \\ 0 & \text{a.o.c} \end{cases}, \tag{4.24}$$

with $\omega_n := \frac{2\pi}{d_n}$ so that $\phi_{np}^{\pm}\left(\pm\Lambda^{-(n+1)}\right) = \phi_{np}^{\pm}\left(\pm\Lambda^{-n}\right)$. Then we can decompose the creation operators $c_k^\dagger$ into their interval-Fourier contributions as

$$c_{k\sigma}^\dagger = \sum_{np} \phi_{np}^{+}(k) c_{np\sigma}^{+\dagger} + \phi_{np}^{-}(k) c_{np\sigma}^{-\dagger} \tag{4.25}$$

with the new creation operators defined as

$$c_{np\sigma}^{\pm\dagger} := \left(c_{np\sigma}^{\pm}\right)^\dagger = \int_{-1}^{1} \mathrm{d}\varepsilon \ \left[\phi_{np}^{+}(\varepsilon)\right]^* c_{\varepsilon\sigma}^\dagger.$$

This decomposition (4.25) is a simple consequence of the orthonormality of the functions defined in (4.24). In addition we can readily proof that $c^{\pm\dagger}_{np\sigma}$-operators satisfy the anti-commutation relations, so that they are rightful fermionic creation operators.

We can now use (4.25) to replace the k-dependent terms in hamiltonian (4.22). Then we obtain

$$\begin{aligned}
\int_{-1}^{1} \mathrm{d}k\, c^{\dagger}_{k\sigma} d_{\sigma} &= \int_{-1}^{1} \mathrm{d}k \left(\sum_{np} \phi^{+}_{np}(k) c^{+\dagger}_{np\sigma} + \phi^{-}_{np}(k) c^{-\dagger}_{np\sigma} \right) d_{\sigma} \\
&= \left(\sum_{np} \left(\int_{-1}^{1} \mathrm{d}k\, \phi^{+}_{np}(k) \right) c^{+\dagger}_{np\sigma} + \left(\int_{-1}^{1} \mathrm{d}k\, \phi^{-}_{np}(k) \right) c^{-\dagger}_{np\sigma} \right) d_{\sigma} \\
&= \left(\sum_{np} \left(\int_{\Lambda^{-(n+1)}}^{\Lambda^{-n}} \mathrm{d}k\, \frac{e^{i\omega_n pk}}{\sqrt{d_n}} \right) c^{+\dagger}_{np\sigma} + \left(\int_{-\Lambda^{-n}}^{-\Lambda^{-(n+1)}} \mathrm{d}k\, \frac{e^{-i\omega_n pk}}{\sqrt{d_n}} \right) c^{-\dagger}_{np\sigma} \right) d_{\sigma} \\
&= \left(\sum_{np} \sqrt{d_n} \delta_p c^{+\dagger}_{np\sigma} + \sqrt{d_n} \delta_p c^{-\dagger}_{np\sigma} \right) d_{\sigma} \\
&= \sqrt{1-\Lambda^{-1}} \sum_{n} \Lambda^{-\frac{n}{2}} \left(c^{+\dagger}_{np\sigma} + c^{-\dagger}_{np\sigma} \right) d_{\sigma}. \qquad (4.26)
\end{aligned}$$

And

$$\begin{aligned}
\int_{-1}^{1} \mathrm{d}k\, k c^{\dagger}_{k\sigma} c_{k\sigma} &= \sum_{n,n',p,p'} \sum_{s,s'=\pm} \left(\int_{-1}^{1} k \mathrm{d}k\, \phi^{s}_{np}(k) \left(\phi^{s'}_{np}(k) \right)^{*} \right) c^{s\dagger}_{np\sigma} c^{s'}_{n'p'\sigma} \\
&= \sum_{n,n',p,p'} \sum_{s,s'=\pm} \left(\frac{\delta_{nn'}\delta_{ss'}}{d_n} \int_{\Lambda^{-(n+1)}}^{\Lambda^{-n}} k \mathrm{d}k\, e^{is\omega_n k(p-p')} \right) c^{s\dagger}_{np\sigma} c^{s}_{np'\sigma} \\
&= \sum_{npp'} \sum_{s=\pm} \left(\frac{s}{2} \Lambda^{-2n} \left(1-\Lambda^{-2} \right) \delta_{pp'} + \frac{1-\delta_{pp'}}{is\omega_n (p-p')} \left[k e^{is\omega_n k(p-p')} \right]_{\Lambda^{-(n+1)}}^{\Lambda^{-n}} \right) \frac{c^{s\dagger}_{np\sigma} c^{s'}_{np'\sigma}}{d_n} \\
&= \frac{1}{2} \left(1+\Lambda^{-1} \right) \sum_{np} \Lambda^{-n} \left(c^{+\dagger}_{np\sigma} c^{+}_{np\sigma} - c^{-\dagger}_{np\sigma} c^{-}_{np\sigma} \right) \\
&\qquad + \sum_{n} \sum_{p \neq p'} \frac{1-\Lambda^{-1}}{2i\pi (p'-p)} \left(c^{+\dagger}_{np\sigma} c^{+}_{np'\sigma} - c^{-\dagger}_{np'\sigma} c^{-}_{np\sigma} \right) e^{\frac{2i\pi(p-p')}{1-\Lambda^{-1}}}. \qquad (4.27)
\end{aligned}$$

Thus, if we replace (4.26) and (4.27) into (4.22) we will obtain a logarithmic discretization of the hamiltonian. The next part will we to map this discretization to an iterative process that is worth for a numerical computations.

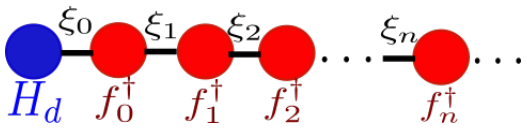

Figure 4.4: Chain-Hamiltonian describing the Anderson model. The chain starts at the initial dot hamiltonian H_d. The $f_m^\dagger$'s are the creation operators at the n^{th}-site of the chain. The ξ_n's describe the magnitude of the interaction between consecutive sites.

Mapping the Anderson model to a Chain-Hamiltonian

We are looking for a model just like the one we have in Figure 4.4. This is because a Chain-Hamiltonian will give an iterative approximation of the Anderson model with an increasing (but still controllable) number of degrees of freedom. This will provide the rightful structure for a numerical diagonalization of the hamiltonian.

To do this, observe from equations (4.26),(4.27) that the QD (d_σ) couples directly only to the operators with $p = 0\left(c_{n0\sigma}^{\pm\dagger}\right)$. The $p \neq 0$ terms will appear in the hamiltonian only because they are coupled to $c_{np\sigma}^{+\dagger}$ in Equation (4.27). Thus, as a first approximation we can neglect all terms in (4.27) with $p \neq 0$. This leaves only the first part of (4.27), so that we can define $c_{n\sigma}^{\pm\dagger} := c_{np\sigma}^{\pm\dagger}$. Let

$$f_{0\sigma}^\dagger = \sqrt{\frac{1-\Lambda^{-1}}{2}} \sum_n \Lambda^{-\frac{n}{2}} \left(c_{n\sigma}^{+\dagger} + c_{n\sigma}^{-\dagger}\right), \text{ so that } \sqrt{2} f_{0\sigma}^\dagger d_\sigma = \int_{-1}^{1} \mathrm{d}k \; c_{k\sigma}^\dagger d_\sigma. \tag{4.28}$$

Note $\left\{f_{0\sigma}^\dagger, f_{0\sigma}\right\} = \frac{1-\Lambda^{-1}}{2} \sum_n 2\Lambda^{-n} = 1$. Replacing this in (4.22)we get

$$H = H_d + D\sum_\sigma \left[\sqrt{\frac{2\Gamma}{\pi D}}\left(d_\sigma^\dagger f_{0\sigma} + f_{0\sigma}^\dagger d_\sigma\right) + \frac{1}{2}\left(1+\Lambda^{-1}\right)\sum_n \Lambda^{-n}\left(c_{n\sigma}^{+\dagger} c_{n\sigma}^{+} - c_{n\sigma}^{-\dagger} c_{n\sigma}^{-}\right)\right].$$

$f_0^\dagger$will represent the first site of the chain-hamiltonian in Figure 4.4 since no other term is coupled to the dot hamiltonian. We also have the coupling term $\xi_0 = \sqrt{\frac{2\Gamma}{\pi D}}$. It is possible to obtain the following $f_m^\dagger$-operators by supposing a solution of the form

$$f_{m\sigma}^\dagger = \sum_n a_{mn}^{+} c_{n\sigma}^{+\dagger} + a_{mn}^{-} c_{n\sigma}^{-\dagger} = \sum_n \sum_{s=\pm} a_{mn}^{s} c_{n\sigma}^{s\dagger}, \tag{4.29}$$

such that they satisfy the anti-commutation relations

$$\left\{f_{m\sigma}^\dagger, f_{m\sigma}\right\} = \delta_{mm'}\delta_{\sigma\sigma'} \;,\; \left\{f_{m\sigma}^\dagger, f_{m\sigma}^\dagger\right\} = \left\{f_{m\sigma}^\dagger, f_{m\sigma}^\dagger\right\} = 0$$

and

$$\frac{1}{2}\left(1+\Lambda^{-1}\right)\sum_{n}\Lambda^{-n}\left(c_{n\sigma}^{+\dagger}c_{n\sigma}^{+}-c_{n\sigma}^{-\dagger}c_{n\sigma}^{-}\right)=\sum_{m=0}^{\infty}\Lambda^{\frac{-m}{2}}\xi_m\left(f_{m\sigma}^{\dagger}f_{m+1,\sigma}+f_{m+1\sigma}^{\dagger}f_{m\sigma}\right). \tag{4.30}$$

It is possible to find a solution for this system using the formula of the right part of equation 4.30. Since the relation is only given between consecutive terms $m, m+1$ and we already have the coefficients for $m=0$ $\left(a_{0n}^{s}=\sqrt{\frac{1-\Lambda^{-1}}{2}}\Lambda^{-\frac{n}{2}}\right)$. Then it is possible to determine the upper coefficients in a recursive way starting from $m=0$. Supposing we can obtain the m^{th}-coefficients (a_{mn}^{s}) and then finding iteratively the coefficients of $m+1$ (a_{mn}^{s}) using the relation given by equation (4.30). This provides a numerical way for obtaining the $f_{m\sigma}^{\dagger}$ operators. In fact in our case, where we actually did important assumptions, the problem can be solved analytically obtaining that the final hamiltonian is given by

$$H=H_d+D\sum_{\sigma}\left[\sqrt{\frac{2\Gamma}{\pi D}}\left(d_{\sigma}^{\dagger}f_{0\sigma}+f_{0\sigma}^{\dagger}d_{\sigma}\right)+\frac{1}{2}\left(1+\Lambda^{-1}\right)\sum_{n=0}^{\infty}\Lambda^{\frac{-n}{2}}\xi_n\left(f_{n\sigma}^{\dagger}f_{n+1,\sigma}+f_{n+1\sigma}^{\dagger}f_{n\sigma}\right)\right]. \tag{4.31}$$

with

$$\xi_n=\frac{1-\Lambda^{-n-1}}{\left(1-\Lambda^{-2n-1}\right)^{\frac{1}{2}}\left(1-\Lambda^{-2n-3}\right)^{\frac{1}{2}}}.$$

The formal recursive-solution of this problem can be found in [16] . Note that equation (4.31) describes the chain hamiltonian model that we where looking for in Figure 4.4. Note that in the limit when $n\longrightarrow\infty$

$$\Lambda^{\frac{-n}{2}}\xi_n\longrightarrow\frac{\Lambda^{\frac{-n}{2}}\left(1-\Lambda^{-n}\right)}{1-\Lambda^{-2n}}\sim\frac{\Lambda^{\frac{-n}{2}}}{1+\Lambda^{-n}},$$

which implies an exponential decaying of the hopping term in the chain.

Iterative Diagonalization in a Single QD process

Now that we have an iterative representation of the Anderson Model Hamiltonian (4.31), lets take a look to how the NRG code would work for a QD. We start with the dot hamiltonian. (Since the D term is always present as a normalizing factor, we are going to avoid this term in future computations and suppose that we are working with unit-less variables ε_d, U and $\Gamma':=\sqrt{\frac{2\Gamma}{\pi D}}$).

$$H_d=\frac{1}{D}\left(\varepsilon_d+\frac{U}{2}\right)d_{\sigma}^{\dagger}d_{\sigma}+\frac{U}{2D}(d_{\sigma}^{\dagger}d_{\sigma}-1)^2. \tag{4.32}$$

Now observe that hamiltonian 4.32 already has a diagonal form in the base $\{|\uparrow\downarrow\rangle, |\uparrow\rangle, |\downarrow\rangle, |0\rangle\}$

$$H_d = \frac{1}{D}\begin{bmatrix} 2\varepsilon_d + \frac{3U}{2} & 0 & 0 & 0 \\ 0 & \varepsilon_d + \frac{U}{2} & 0 & 0 \\ 0 & 0 & \varepsilon_d + \frac{U}{2} & 0 \\ 0 & 0 & 0 & \frac{U}{2} \end{bmatrix}.$$

Lets define $H_{-1} = \Lambda^{\frac{-1}{2}} H_d$. Adding the first chain interaction to H_d we obtain a new hamiltonian of the form

$$H_0 = \Lambda^{\frac{1}{2}} H_{-1} + \Gamma' \left(d^\dagger_\sigma f_{0\sigma} + f^\dagger_{0\sigma} d_\sigma \right). \tag{4.33}$$

The Hilbert space for this hamiltonian has to be extended to include the 4 degrees of freedom of the $f^\dagger_{0\sigma}$ particles which are also given by $\{|\uparrow\downarrow\rangle, |\uparrow\rangle, |\downarrow\rangle, |0\rangle\}$. Therefore the total Hilbert space for H_0 is given by a base of the form

$$|s_1\rangle|s_2\rangle := |s_1\rangle \otimes |s_2\rangle \text{ with } |s_{1,2}\rangle \in \{|\uparrow\downarrow\rangle, |\uparrow\rangle, |\downarrow\rangle, |0\rangle\}.$$

We obtain an space of dimension $4 \times 4 = 16$. Now before adventuring to write the Hamiltonian for H_0 as a 16×16-matrix note that H_0 preserves particle number N and the total spin S. Therefore we can use N and S as quantum numbers and generate the Hamiltonian H_0 in blocks. We will observe that the terms in the diagonal will correspond to the eigenvalues of H_{-1} for the first space. The non-diagonal terms are the result of the hopping interactions with the first site.

$H_{N=0,S=0}$:

$$|0\rangle|0\rangle \to \left[\tfrac{U}{2}\right]$$

$H_{N=4,S=0}$:

$$|\uparrow\downarrow\rangle|\uparrow\downarrow\rangle \to \left[2\varepsilon_d + \tfrac{3U}{2}\right]$$

$H_{N=1,S=\frac{1}{2}}$:

$$\begin{array}{l} |\uparrow\rangle|0\rangle \to \\ |0\rangle|\uparrow\rangle \to \end{array} \begin{bmatrix} \varepsilon_d + \frac{U}{2} & \Gamma' \\ \Gamma' & \frac{U}{2} \end{bmatrix}$$

$H_{N=1,S=\frac{-1}{2}}$:

$$\begin{array}{l} |\uparrow\rangle|0\rangle \to \\ |0\rangle|\uparrow\rangle \to \end{array} \begin{bmatrix} \varepsilon_d + \frac{U}{2} & \Gamma' \\ \Gamma' & \frac{U}{2} \end{bmatrix}$$

$H_{N=2,S=-1}$:

$$|\downarrow\rangle|\downarrow\rangle \to \left[\varepsilon_d + \tfrac{U}{2}\right]$$

$H_{N=2,S=1}$:

$$|\uparrow\rangle|\uparrow\rangle \to \left[\varepsilon_d + \tfrac{U}{2}\right]$$

$H_{N=2,S=0}$:

$$\begin{array}{l} |\uparrow\downarrow\rangle|0\rangle \to \\ |\uparrow\rangle|\downarrow\rangle \to \\ |\downarrow\rangle|\uparrow\rangle \to \\ |0\rangle|\uparrow\downarrow\rangle \to \end{array} \begin{bmatrix} 2\varepsilon_d + \frac{3U}{2} & \Gamma & -\Gamma & 0 \\ \Gamma & \varepsilon_d + \frac{U}{2} & 0 & \Gamma \\ -\Gamma & 0 & \varepsilon_d + \frac{U}{2} & -\Gamma \\ 0 & \Gamma & -\Gamma & \frac{U}{2} \end{bmatrix}$$

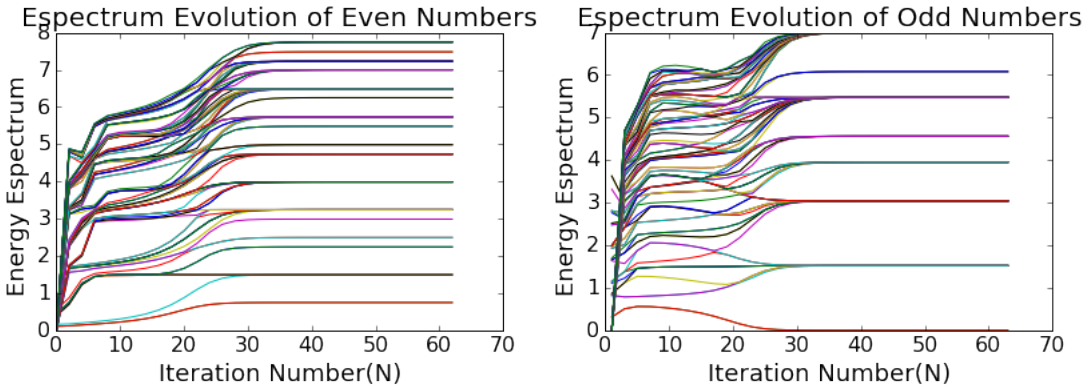

(a) N takes only even values

(b) N run only through odd values

Figure 4.5: Evolution of the QD-spectrum vs number of iterations of the code for $U = 0.5$, $e_d = -0.25$, $\Gamma = 2.82 \times 10^{-2}$.

$$H_{N=3,S=\frac{1}{2}}: \qquad H_{N=3,S=\frac{-1}{2}}:$$

$$\begin{array}{l} |\uparrow\downarrow\rangle|\uparrow\rangle \rightarrow \\ |\uparrow\rangle|\uparrow\downarrow\rangle \rightarrow \end{array} \begin{bmatrix} \varepsilon_d + \frac{U}{2} & -\Gamma' \\ -\Gamma' & \frac{U}{2} \end{bmatrix} \qquad \begin{array}{l} |\uparrow\downarrow\rangle|\downarrow\rangle \rightarrow \\ |\downarrow\rangle|\uparrow\downarrow\rangle \rightarrow \end{array} \begin{bmatrix} \varepsilon_d + \frac{U}{2} & -\Gamma' \\ -\Gamma' & \frac{U}{2} \end{bmatrix}$$

Finally, we proceed to diagonalize H_0 by blocks $H_{N,S}$. The resulting eigenvectors will be characterized by both quantum numbers so that we can write them in the form $|N,S,i\rangle$ with i takes as many values as the degeneracy of its block. For higher values of N, the general formula for equation (4.33) looks as

$$H_{N+1} = \Lambda^{\frac{1}{2}} \left[H_N + \frac{1}{2}\left(1+\Lambda^{-1}\right) \xi_N \left(f^{\dagger}_{N\sigma} f_{N+1,\sigma} + f^{\dagger}_{N+1\sigma} f_{N\sigma} \right) \right]. \tag{4.34}$$

We now proceed by induction supposing that for each N the Hamiltonian H_N is already diagonalized and the eigenvectors are organized in states with labels $|N,S,i\rangle$. The next step will be to add the 4-Hilbert space corresponding to $f_{N+1,\sigma}$ organized the eigenvectors according to the quantum numbers $|N',S',i\rangle$ and proceed to diagonalize by blocks the new Hamiltonian. Apart of it, the code must have a cutoff to the number of states.

This NRG code was previously implemented in C++ language by the advisor of this thesis. In Figure 4.5 we observe the evolution of the spectrum of the Hamiltonian according to the number of iterations of the code. As we can appreciate, this evolution converges for even and odd number around $N = 30$.

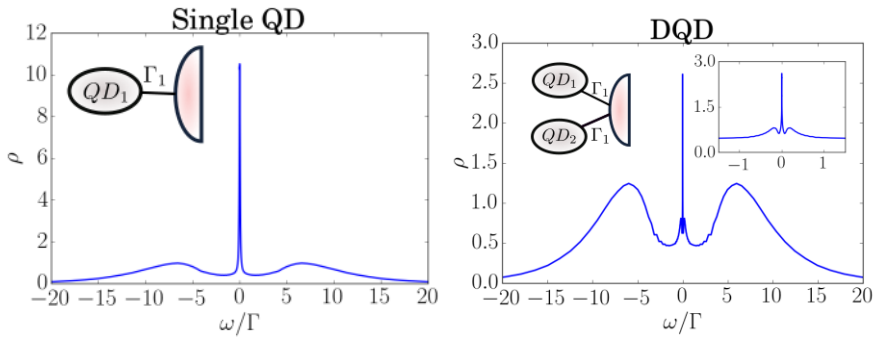

(a) (b) $\Gamma_2 = \Gamma_1$. Inset: Low energy DOS.

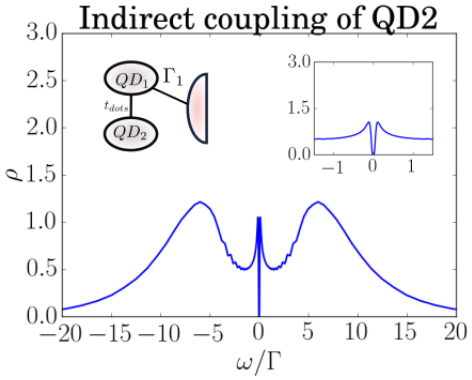

(c) $t_{dots} = 0.689\Gamma$. Low energy DOS.

Figure 4.6: Density of states in QD1 predicted by NRG at each case. The insets show the. Note that figure a) is in a different scale due to a major central peak ..

Source: *By the Author*

4.2.1 Density Matrix Renormalization Group (DM-NRG)

To compute dynamical quantities [19] like the density of states we used the density matrix renormalization group approach DMNRG [20].

4.2.2 NRG for a double quantum dot

The initial Hamiltonian for the double quantum dot model has initial dimension of 16. While the symmetries in this Hamiltonian are exactly the same than the ones in the single QD case that we presented in the last section, we decided to use another model to solve this system. This system was simulated using the code for a DQD-Majorana coupling presented on chapter 5 by setting the Majorana couplings to $t_1 = t_2 = 0$. The viability of these result and its correspondence with previous works is an important test that supports the conclusions of our code.

We ran the NRG code for the DQD with the coulomb term fixed at

$$U_1 = U_2 = 17.7305 \tag{4.35}$$

and are set up to emulate the same configurations in Figure 4.2.

The single QD attached to a metallic lead is a particular case of the double quantum dot model, where the second dot is not attached $\Gamma_2 = t_{dots} = 0$. Figure 4.6 shows the NRG results for this case. The three plots show the external Coulomb peaks at $e_1 = \frac{U}{2} \sim 8.62\Gamma_1$, which represent the DOS of the energy levels. In addition Figure 4.6a shows a central peak at the Fermi energy. **This is the Kondo Peak**.

In Figure 4.6b we observe the DOS when the two QDs are symmetrically attached. At low energies, the inset shows the appearance of two satellite peaks representing the Ruderman-Kittel-Kasuya-Yosida (RKKY) interaction. This is an anti-ferromagnetic coupling that appears in the interacting case due to the strong correlations between both dots. A detailed explanation of the appearance of these new states is included in section Appendix B.

The most interesting case is in Figure 4.6c. As we already observed in the non-interacting case, the interference with the second dot completely destroys the Kondo peak. This effect is observed at low energies closed to $t_{dots} = 0.689\Gamma$. The paper describing this result was a central part of one of my advisor's project. This result encouraged me to formulate the following question. What happens if we attached a Majorana mode to one of these dots?. Would it e destroyed by interference or it will survive to it. Answering this question is one of the mean objectives of chapter chapter 5.

Chapter 5

Coupling the Majorana Zero Mode to a Double Quantum Dot

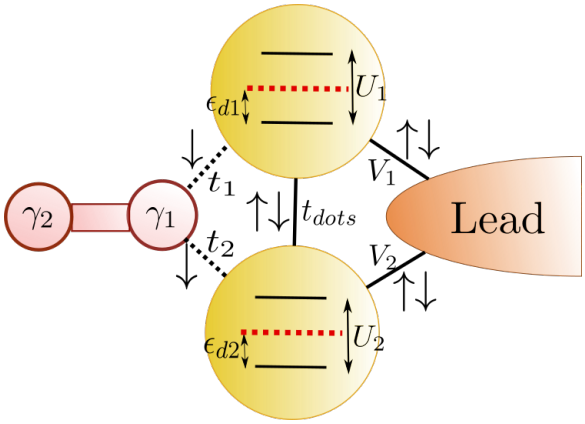

Figure 5.1: General model. Source: *By the Author*

The idea of using Majorana islands formed by QDs coupled to topological superconducting wires has recently turned on new lights into the fabrication of of quantum architectures [21, 22]. The main insight of this method is that todayâs precise experimental control over the parameters of QDs -energy levels, tunneling couplings, etc.- offers the unique possibility of manipulating the Majorana modes inside multi-dot systems. The simplest case where Majorana manipulation is possible is in a double quantum dot. So far, no complete analysis of this basis case has been done. The purpose of this chapter is to fill this gap by realizing a full quantum transport study of the effects of coupling a Majorana mode with a double quantum dot. For this, we combine the ballistic transport and the NRG approach developed in chapter 4.

We consider the model in Figure 5.1 which can be obtained from the combination of Hamiltonians of a QD-Majorana (**??**) and a DQD (4.9). The Hamiltonian

$$H=\sum_{i=1}^{2}\sum_{k,\sigma}\left(\varepsilon_i+\frac{U_i}{2}\right)d_{i\sigma}^{\dagger}d_{i\sigma}+\frac{U_i}{2}(d_{i\sigma}^{\dagger}d_{i\sigma}-1)^2+t_i(\gamma d_{i,\downarrow}+d_{i,\downarrow}^{\dagger}\gamma)+V_i d_{i\sigma}^{\dagger}c_{k\sigma}+V_i^{*}c_{k\sigma}^{\dagger}d_{i\sigma}. \quad (5.1)$$

5.1 Non-interacting case

In order to understand the physical properties of this model, we probed a set of thought processes. The main variable in this analysis is the density of states. We will observe its evolution on both QDs under the tuning of the model parameters such as the majorana couplings (t_1, t_2) , gate voltages ($\varepsilon_1, \varepsilon_2$) and the inter dot coupling (t_{dots}). With these processes intend to show whether it is possible to "manipulate" the majorana modes inside the dots by tuning the established parameters. The number of possible combinations of parameters is huge and not all of them lead to important results. So on, we used the ballistic transport to select which arrangements could bring novel results. The most interesting models were simulated with NRG in the interacting case Figure 5.3.

5.1.1 The Green function:

This new model is a combination the DQD graph (Figure 4.1) with the Majorana-QD graph **??**.b). We can use the trick in **??** to get rid of the of the Green function $G_{f_\downarrow, d_1^\dagger}(\omega)$ for the second Majorana operator. This allows us to obtain the following transport equations

$$\begin{bmatrix} \omega-\varepsilon_1 & -V_1^* & -t_{dots} & -T_1 & 0 & 0 & 0 \\ -V_1 & \omega-\varepsilon_k & -V_2 & 0 & 0 & 0 & 0 \\ -t_{dots}^* & -V_2^* & \omega-\varepsilon_2 & -T_2 & 0 & 0 & 0 \\ -T_1^* & 0 & -T_2^* & \omega-\varepsilon_M & -T_2^* & 0 & -T_1 \\ 0 & 0 & 0 & -T_2 & \omega+\varepsilon_2 & V_2^* & t_{dots}^* \\ 0 & 0 & 0 & 0 & V_2 & \omega+\varepsilon_k & V_1 \\ 0 & 0 & 0 & -T_1 & t_{dots} & V_1^* & \omega+\varepsilon_1 \end{bmatrix} \begin{bmatrix} G_{d_{\mathbf{1}\downarrow}, d_{1\downarrow}^\dagger}(\omega) \\ G_{c_{k\downarrow}, d_{1\downarrow}^\dagger}(\omega) \\ G_{d_{2\downarrow}, d_{1\downarrow}^\dagger}(\omega) \\ G_{f_\downarrow, d_{1\downarrow}^\dagger}(\omega) \\ G_{d_{2\downarrow}^\dagger, d_{1\downarrow}^\dagger}(\omega) \\ G_{c_{k\downarrow}^\dagger, d_{1\downarrow}^\dagger}(\omega) \\ G_{d_{1\downarrow}^\dagger, d_{1\downarrow}^\dagger}(\omega) \end{bmatrix} = \begin{bmatrix} 0 \\ 0 \\ 0 \\ 0 \\ 0 \\ 0 \\ 1 \end{bmatrix}, \tag{5.2}$$

where $T_i = \frac{t_1}{\sqrt{\omega+\varepsilon_M}}$.

The graph representing this equation is Figure 5.2.a). Using the algorithm in subsection 4.1.2 we start to popping the vertexes $c_k, c_k^\dagger, d_{2,\downarrow}$ and $d_{2,\downarrow}^\dagger$ in that order. The energies associated to $d_{1,\downarrow}$ and $d_{1,\downarrow}^\dagger$ will be similar to the energy of the DQD (4.15) giving

$$\varepsilon_{DQD}^{\pm} = \pm\varepsilon_1 + \sum_{\mathbf{k}} \frac{V_1 V_1^*}{\omega - \varepsilon_{\mathbf{k}}} + \frac{\left\| \pm t_{dots} + \sum_{\mathbf{k}} \frac{V_1 V_2^*}{\omega-\varepsilon_{\mathbf{k}}} \right\|^2}{\omega \pm \varepsilon_2 - \sum_{\mathbf{k}} \frac{V_2 V_2^*}{\omega-\varepsilon_{\mathbf{k}}}}. \tag{5.3}$$

There is also a correction in the couplings between the Majorana mode and $d_{1,\downarrow}$, $d_{1,\downarrow}^\dagger$ given by

$$T_\pm = \pm t_1 \pm t_2 \frac{\left(\pm t_{dots} + \sum_{\mathbf{k}} \frac{V_1 V_2^*}{\omega-\varepsilon_{\mathbf{k}}} \right)}{\omega \pm \varepsilon_2 \pm \sum_{\mathbf{k}} \frac{V_2 V_2^*}{\omega-\varepsilon_{\mathbf{k}}}}. \tag{5.4}$$

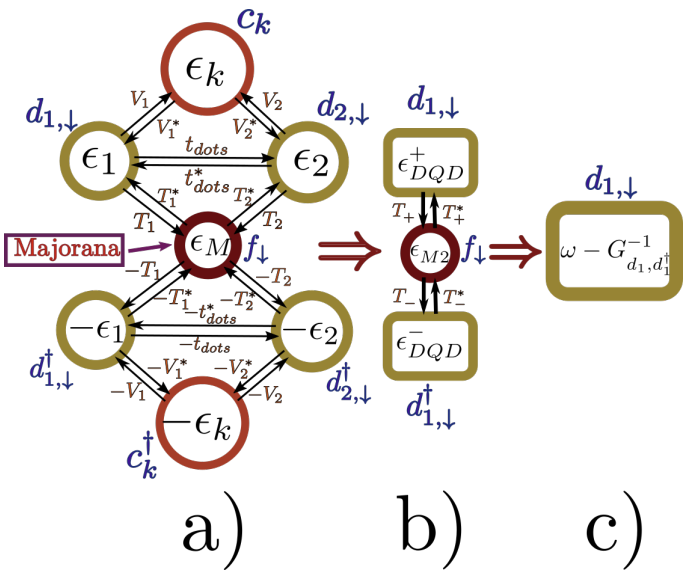

Graph.png

Figure 5.2: Graph method applied to a DQD coupled to a Majorana zero mode. a) Initial stage. b) Popped vertexes $c_k^\dagger$, c_k, $d_{2,\downarrow}$, $d_{2,\downarrow}^\dagger$ in that order. c) Popped vertexes $d_{1,\downarrow}^\dagger$ and $f_\downarrow$, the final energy is $\omega - G_{d_1,d_1^\dagger}(\omega)$.

Source: *By the Author*

In addition since the Majorana is in contact with dot 2, there is an extra-term appearing in the Majorana energy given by

$$\varepsilon_{M2} = \omega - \varepsilon_M - \frac{\frac{\omega}{\omega+\varepsilon_M}\|t_2\|^2}{\omega - \varepsilon_2 - \sum_{\mathbf{k}} \frac{V_2 V_2^*}{\omega - \varepsilon_{\mathbf{k}}}} - \frac{\frac{\omega}{\omega+\varepsilon_M}\|t_2\|^2}{\omega + \varepsilon_2 - \sum_{\mathbf{k}} \frac{V_2 V_2^*}{\omega + \varepsilon_{\mathbf{k}}}}. \tag{5.5}$$

It only remains to pop out vertexes $d_1^\dagger$ and $f_\downarrow$ in that order to obtain the green function

$$G_{d_{1\downarrow},d_{1\downarrow}^\dagger}(\omega) = \frac{1}{\omega - \varepsilon_{DQD}^+ - \frac{\|T_+\|^2}{\omega - \varepsilon_{M2} - \frac{\|T_-\|^2}{\varepsilon_{DQD}^-}}}. \tag{5.6}$$

This simple formula summarizes the transport information through the first dot of the non-interacting Majorana-DQD system. To compute the DOS we just need to replace once again $\sum \frac{V_1 V_1^*}{\omega - \varepsilon_k} = -i\Gamma_1$ as performed in subsection 4.1.1. By plotting the final DOS in Mathematica we were able to observe the transitions of the Majorana mode while manipulating the model parameters.

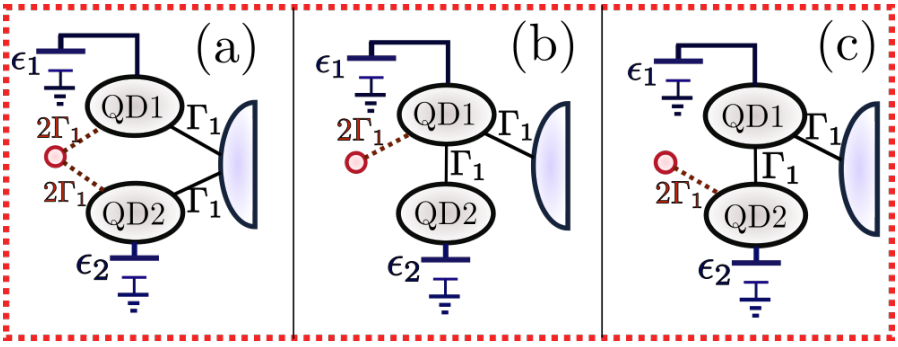

Figure 5.3: . Source: *By the Author*

5.1.2 Theoretical results of the interacting system

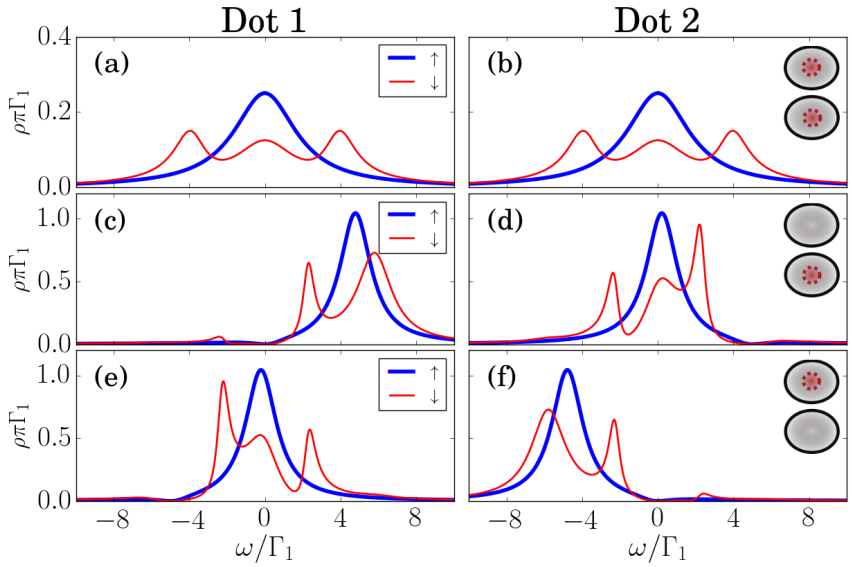

Figure 5.4: Density of states in dots 1(Left) and 2(Right) for the model Figure 5.3. (a). First line (a),(b): $\varepsilon_1 = \varepsilon_2 = 0$. Second line (c),(d): $\varepsilon_1 = 5\Gamma_1$, $\varepsilon_2 = 0$. Third line (e),(f): $\varepsilon_2 = -5\Gamma_1$, $\varepsilon_1 = 0$. Blue bold lines: Spin-$\uparrow$ DOS. Red thin lines: Spin-$\downarrow$ DOS. The inset at the upper-right corner of each line indicates which dots exhibit Majorana signature, which is represented by a red dashed circle inside the dot.

In this part we will discuss the three models in figure Figure 5.3 which are particularly interesting for the exotic behavior of their Majorana signature. The parameters (t_1, t_2, t_dots) are fixed

in these three models and we will take ε_1 and ε_2 as variables. The first model(a), represents a symmetric coupling of the DQD with the lead and the Majorana mode. In models (b) and (c) the second dot is indirectly coupled to the system through the first dot. As already analyzed in subsection 4.1.3, the quantum interference generated by this coupling will destroy the central peak. The Majorana fermion can be either connected to the first dot (b) or to the second dot (c). The system will exhibit different Majorana signatures depending on which dot is connected to the Majorana zero mode.

On each case we observe three different situations.

- First Row: Zero bias. No gate $\varepsilon_1 = \varepsilon_2 = 0$.
- Second Row: We turn on the first dot's gate voltage $\varepsilon_1 = 5\Gamma_1, \varepsilon_2 = 0$.
- Third Row: We turn on the second dot's gate voltage $\varepsilon_2 = -5\Gamma_1, \varepsilon_1 = 0$.

The density of states for the setup in Figure 5.3.(a) is shown in Figure Figure 5.4. Since the model is non-interacting, spin-$\uparrow$ and spin-$\downarrow$ models are independent. The spin-$\downarrow$ DOS (dashed line) shows the effects caused by the Majorana zero-mode in comparison with the spin-$\uparrow$ results (solid line). In the particle hole symmetric (first line) the DOS is equal in both dots. Note that that the spin-$\downarrow$ DOS is the half of the spin-*DOS* at the fermi energy $\rho_\downarrow(0) = \rho_\uparrow(0)$. This Majorana signature is similar to the one observed in the single dot case [4]. We may conclude that the Majorana tunnels inside both dots. If a positive or negative gate voltage is induced in one of the dots, as shown in the second and third row of Figure Figure 5.4, the Majorana zero mode vanishes. Looking to the other dot we can also observe that the Majorana signature in the other dot recovers the form observed in the single dot-Majorana model. Thus, by activating the gate voltage in one of the dots it is possible to induce the majorana mode to leave to the other dot.

If the second dot is not directly connected to the lead the induced tunneling between both dots generates a path difference that destroys the central peak (See FIGFigure 5.8 spin-$\uparrow$ line). We can then proceed to connect the Majorana to each one of these dots. FIG.Figure 5.8 shows the results of connecting the MZM to the first dot. Note that at zero-bias, quantum interference destroys the Majorana mode in the first dot. However, in the second dot the spin-$\downarrow$ DOS is the half of the spin-$\uparrow$ DOS at the Fermi energy, which is a clear Majorana signature. Hence, in this kind of arrangement the Majorana mode is allocated in the second dot. Figure 5.8(e),(f) show that it is possible to reestablish the initial Majorana signature in the first dot by applying a gate voltage to the second dot. On the other hand, turning on the first dot's gate voltage does not lead to a meaningful change in the Majorana signature Figure 5.8(c),(d). While the spin-$\downarrow$ DOS in the first dot is still 0 at the Fermi energy, the second dot shows a 0.5-height zero mode. Although the spin-$\uparrow$ DOS does not double the density of states any more, this signal is robust and equal in height to a Majorana signature which supports our claim that it is indeed a Majorana mode. If the Majorana mode is connected to the first dot, this interference will destroy the Majorana signature in the first dot. Interestingly, it is possible to observe a clear Majorana signature in the

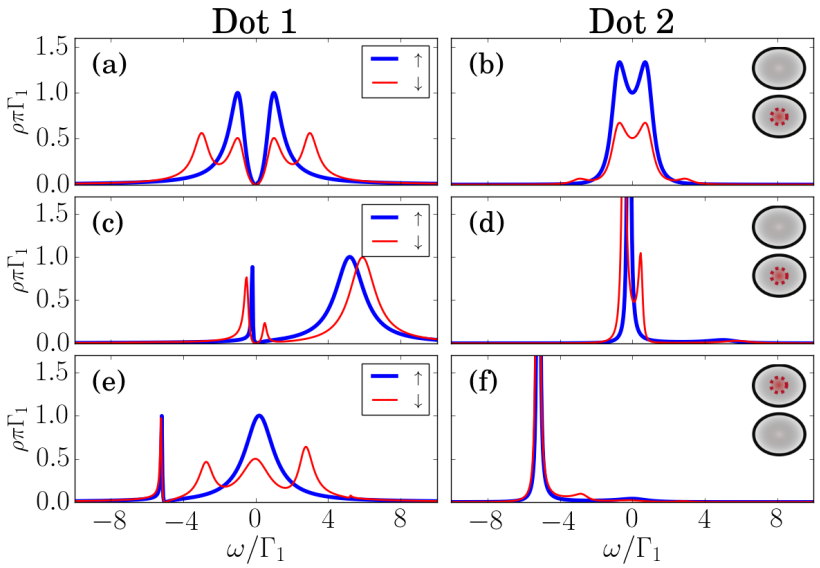

Figure 5.5: Density of states in dots 1(Left) and 2(Right) for the model Figure 5.3. (b). First line (a),(b): $\varepsilon_1 = \varepsilon_2 = 0$. Second line (c),(d): $\varepsilon_1 = 5\Gamma_1$, $\varepsilon_2 = 0$. Third line (e),(f): $\varepsilon_2 = -5\Gamma_1$, $\varepsilon_1 = 0$. Blue bold lines: Spin-↑ DOS. Red thin lines: Spin-↓ DOS. The inset at the upper-right corner of each line indicates which dots exhibit Majorana signature, which is represented by a red dashed circle inside the dot.

second dot characterized by a half central peak in the spin-*dw* DOS. While turning on the first dot gate voltage seems to destroy this Majorana signature, tuning the second dots gate voltage returns the Majorana signature to the first dot.

We now get into the final case that is when the Majorana mode is coupled to the second dot which is indirectly attached to the lead through the first dot. In this case Figure 5.6(a)(b) shows that the Majorana signature is present in both dots, despite the Majorana is not directly coupled to the first dot. Morever we can observe that the spin-↓ DOS is equal to 0.5 at the Fermi energy while the spin-↑ peak has been destroyed by the interference. After turning on the first gate voltage we observe that the Majorana signature is destroyed in both dots Figure 5.6(c)(d). This is totally opposite to what occurs when turning on the second dot voltage where we observe an stable 0.5 Majorana signature at the Fermi energy of both dots Figure 5.6(e)(f).

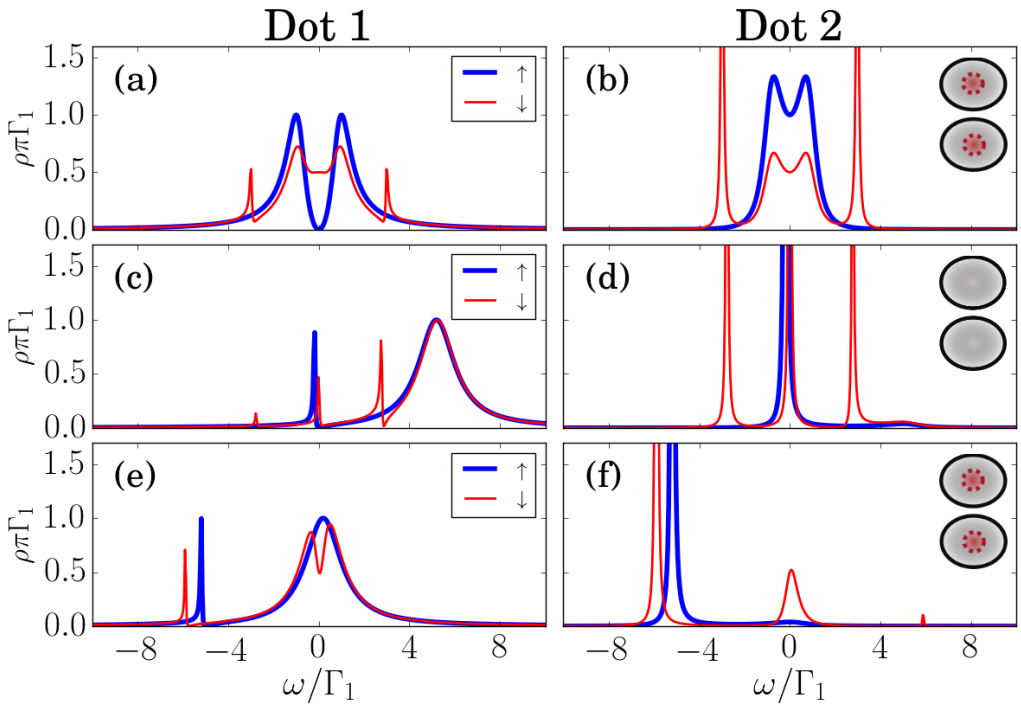

Figure 5.6: Density of states in dots 1(Left) and 2(Right) for the model Figure 5.3. (c). First line (a),(b): $\varepsilon_1 = \varepsilon_2 = 0$. Second line (c),(d): $\varepsilon_1 = 5\Gamma_1$, $\varepsilon_2 = 0$. Third line (e),(f): $\varepsilon_2 = -5\Gamma_1$, $\varepsilon_1 = 0$. Blue bold lines: Spin-↑ DOS. Red thin lines: Spin-↓ DOS. The inset at the upper-right corner of each line indicates which dots exhibit Majorana signature, which is represented by a red dashed circle inside the dot.

5.1.3 a) Removing Kondo and Majorana with QD-interference

Note *Text coming soon*

Graficos/t2=0.png

Figure 5.7: Density of states in both dots of the case where the only the first QD is attached to both Majorana and Lead (Fig.**??** second column) . Solid lines: Spin-↑ DOS. Dashed lines: Spin-↓ DOS.

Graficos/t2=0.png

Figure 5.8: Density of states in both dots of the case where the only the first QD is attached to both Majorana and Lead (Fig.**??** second column) . Solid lines: Spin-↑ DOS. Dashed lines: Spin-↓ DOS.

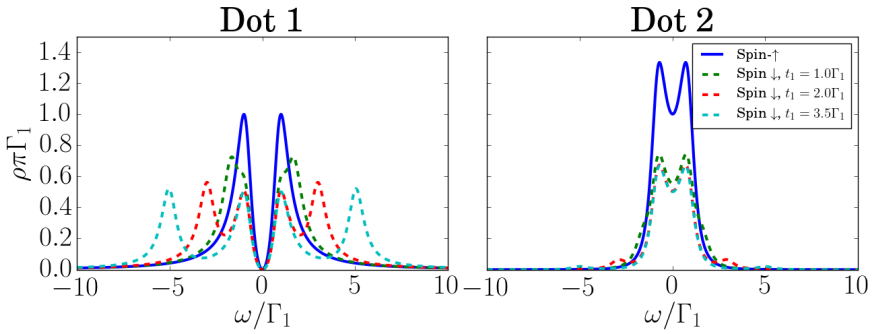

Figure 5.9: Source: *By the Author*

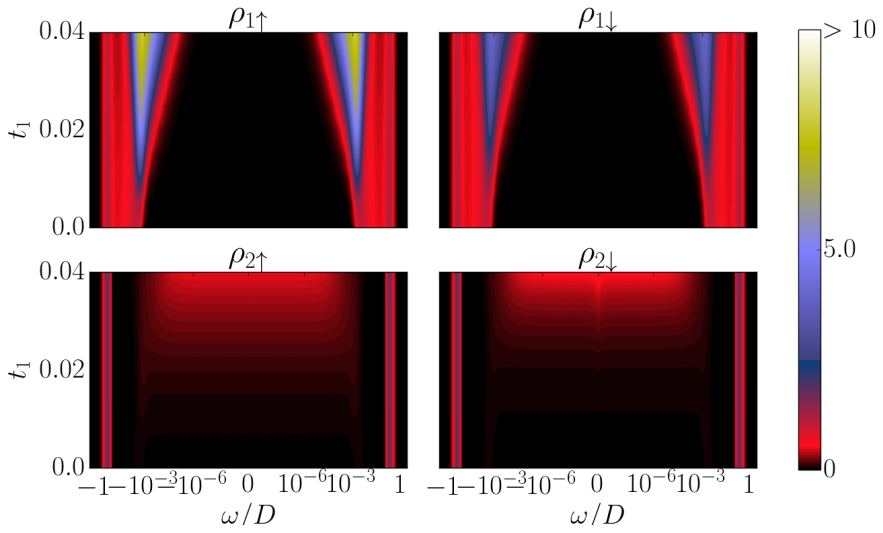

Figure 5.10: Source: *By the Author*

5.1.4 b) Indirect Majorana after Removing Kondo with QD-interference

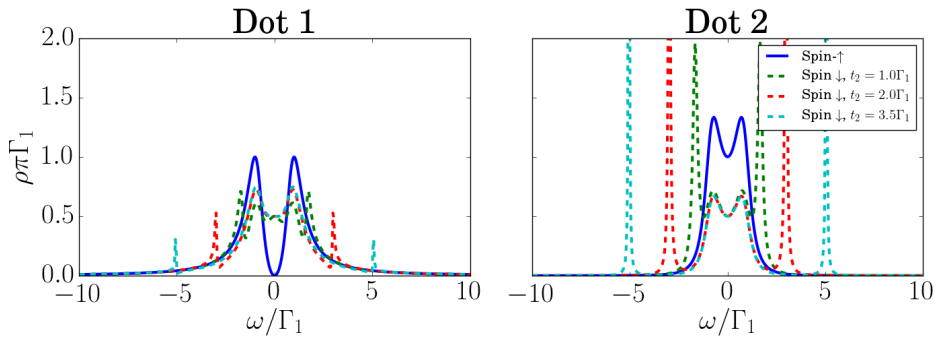

Figure 5.11: Source: *By the Author*

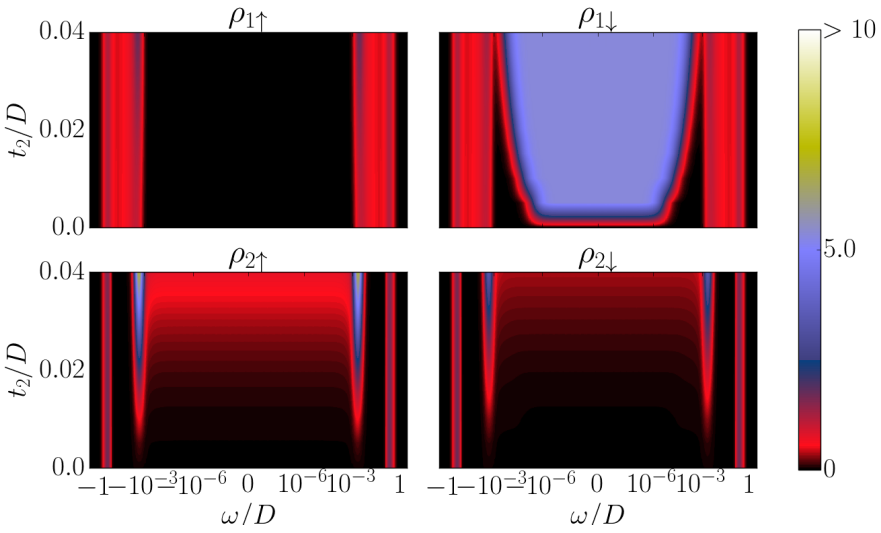

Figure 5.12: Source: *By the Author*

c) Attaching the Majorana mode to the DQD (Tuning $t_1 = t_2$)

Parameters:

$$\Gamma \sim 2.83 * 10^{-2} D, t_{dots} = 0, U_{1,2} = -2\varepsilon_{1,2} = 0.5$$

$$t_1 = t_2 \in [0\ ,\ 2.5 * 10^{-2} D]$$

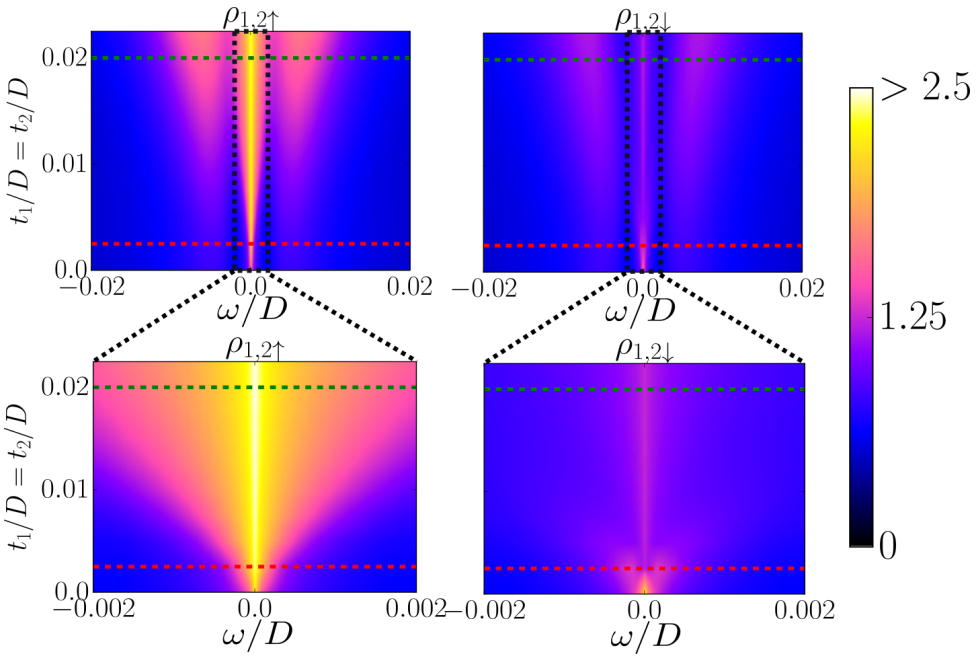

Figure 5.13: Evolution of the DOS of both QDs through $t_1 = t_2$ tuning. UP: Energy scale $\omega \sim 10^{-2} D$. DOWN: Energy scale $\omega \sim 10^{-3} D$. LEFT: Spin $\uparrow$. RIGHT: Spin $\downarrow$.

The first process consists in attaching the Majorana mode to both Quantum Dots symmetrically. For this, we scale up the coupling parameter $t_1 = t_2$ from 0 (Decoupled) to 0.02 (Completely coupled).The other parameters where chosen with an equilibrium between the dot energy and Coulomb repulsion ($\varepsilon_{1,2} = -\frac{U_{1,2}}{2}$) and without inter-dot coupling $t_{dots} = 0$. These circumstances guarantee that the system preserves Particle Hole Symmetry (PHS). Thus the Density of States (DOS) of particles and holes remains equal at all instances ($\rho(-\omega) = \rho(\omega)$).

In the case where the Majorana is detached from the DQD ($t_1 = t_2 = 0$), the system favors the appearance of a three-peak at low energies as it is shown in Figure 5.14 . The central peak is produced only by the Kondo effect and the two other satellite peaks are the result of a strong correlation between both dots caused by the indirect exchange of quantum states through the

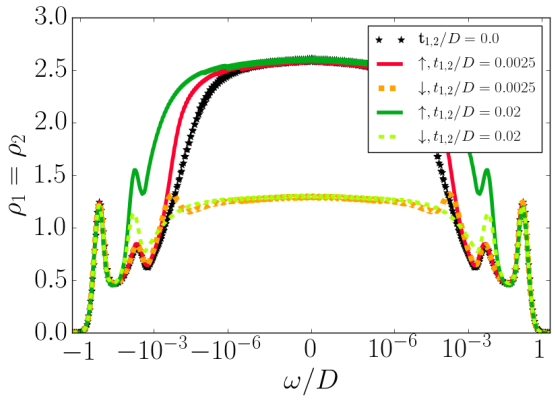

Figure 5.14: Density of states at each QD of the horizontal dashed cuts in Figure 5.13. The energy is in logarithmic scale. For $t_1 = t_2 > 0$ spin-$\uparrow$ and spin-$\downarrow$ DOS split near the order of $|\omega| \sim t_1, 2$. At the Fermi energy $(\omega = 0)$ $\rho_\uparrow = 2\rho_\downarrow$ due to the presence of the MZM in both QDs.

Lead Appendix B.

Once the MZM the spin-$\uparrow$ and spin-$\downarrow$ DOS split at low energies due to the new spin-$\downarrow$ transport channel through the Majorana mode. The spin-$\downarrow$ DOS at the Fermi energy $(\omega = 0)$ decays to the half of the spin-$\uparrow$ DOS $\rho_\downarrow = \frac{\rho_\uparrow}{2}$. By symmetry in the dot parameters this event occurs equally for both QDs. We adopt this fact as a Majorana signature. Hence we obtain that the MZM leaks inside both quantum dots.

There is also an additional effect caused by the indirect exchange between the QDs through the Majorana mode . The consequences of this effect depend on the energy range of the Majorana couplings $t_1 = t_2$. :

1. If $t_1 = t_2 \ll \Gamma$ two more satellites are formed at very low energies ($\sim t_1$) in the spin-$\downarrow$ DOS (See Figure 5.13 Spin-down $\omega \sim 10^{-3}D$). (See Figure 5.13 Spin $\uparrow$, $\omega \sim 10^{-3}D$).

2. If $t_1 = t_2 \sim \Gamma$, the MZM contributes to the the growth of the spin-up satellites in the DOS. This effect produces the splitting between the spin-up and spin-down DOS. (See Figure 5.13 Spin-$\downarrow$, $\omega \sim 10^{-2}D$).

5.1.5 e) Transferring the MZM through gate voltage shifting ε_2.

Parameters:

$$\Gamma \sim 2.83 * 10^{-2}D, t_{dots} = 0, U_{1,2} = -2\varepsilon_1 = 0.5, t_1 = t_2 = 0.0025$$

$$\varepsilon_2 \in [-0.25\ , -0.05]$$

This process starts with the DQD coupled symmetrically to the Majorana mode, just as in section 5.1.4. The idea of this process is to break PHS by increasing the energy of the second QD ε_2. This procedure should induce the Majorana to tunnel only into the first dot.

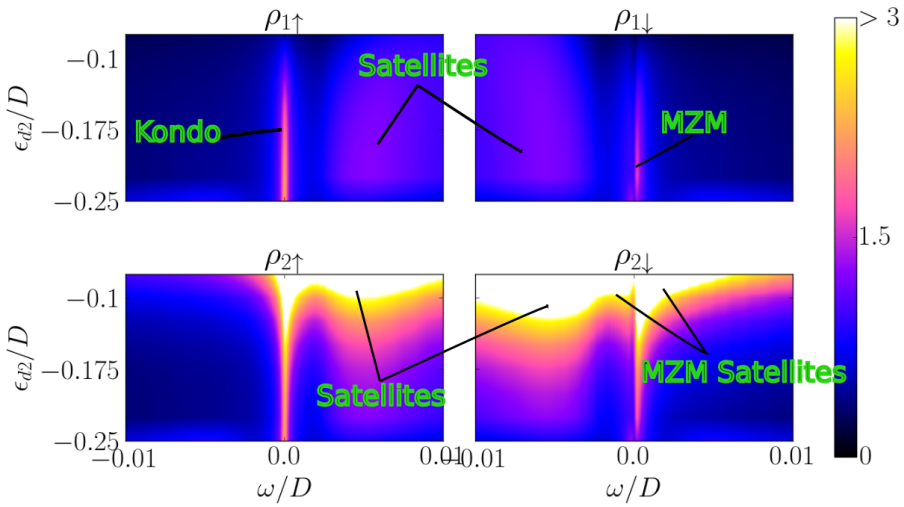

Figure 5.15: Evolution of the DOS of both QDs through the ε_2 tuning. UP: QD1. DOWN: QD2. LEFT: Spin ↑. RIGHT: Spin ↓.

In Figure 5.15 we observe that both, the Kondo and the MZM peaks are preserved in the first QD as well as the majorana signature (See Figure 5.16) when ε_2 is scaled up to -0.1. However, PHS breaking will favor the growth of the spin-↑ hole $(w > 0)$ satellite and the spin-↓ particle $(w < 0)$ satellite.

In the second QD the DOS increases abruptly for both spins.The majorana signature is rapidly when lost . Hence, with this set-up it is actually possible to induce the Majorana to preferably tunnel QD1 in despite of QD2.

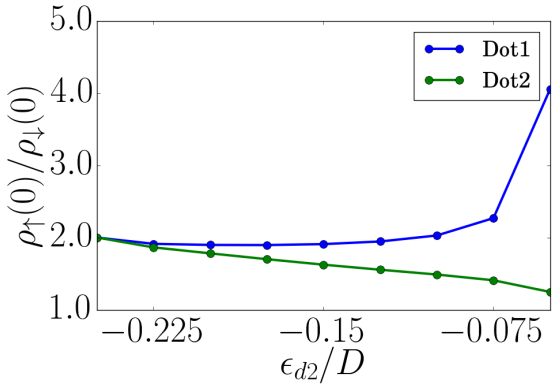

Figure 5.16: As described in section 5.1.4 the relation $\frac{\rho_\uparrow(0)}{\rho_\uparrow(0)} = 2$ constitutes a Majorana Signature . This picture evaluates shows the evolution of the relation $\frac{\rho_\uparrow(0)}{\rho_\uparrow(0)}$ for both QDs. While QD2 losses rapidly the Majorana signature, QD1 maintains it till $\varepsilon_2 \sim -0.1$.

5.2 Particle-Hole symmetric shifting of $\varepsilon_2 = \frac{U}{2}$.

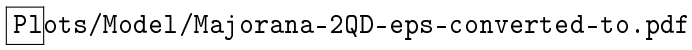

Figure 5.17: $U_1 = -2\varepsilon_{d1} = 0.5$, $\Gamma_1 = \Gamma_2$, $t_1 = t_2 = 0.02$. Variable $\varepsilon_{d2} = \frac{U_2}{2}$

Figure 5.18: Evolution of the QDs' DOS for the model in Figure 5.17

We start again with the symmetric model with both QDs coupled to the Majorana mode, but this time the evolution is performed over $\varepsilon_2 = \frac{U}{2}$, such that the model is always Particle-Hole symmetric. This situation is very different from the previous model (subsection 5.1.5) since the decaying of $U2$ equalizes the effect of increasing the dot energy. In Figure 5.18 we observe that the DOS of QD2 increases while the QD1's DOS decreases, just as it happened in subsection 5.1.5 . However, the Majorana signature remains at 2 for both dots , meaning that the Majorana is not preferably induced to tunnel to any QD despite the lose of symmetry in the dot energy.

5.3 Shifting t_2

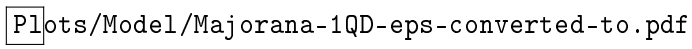

Figure 5.19: $U_1 = U_2 = -2\varepsilon_{d1} = -2\varepsilon_{d2} = 0.5$, $\Gamma_1 = \Gamma_2$, $t_1 = 0.02$. Variable t_2

In Figure 5.20 and Figure 5.20 we observe the evolution of DOS in the case where the second dot is smoothly connected to the Majorana, which is already attached to the first dot. The hopping parameter t_2 scales up to $0.015D$ where the model reaches the symmetry $t_2 = t_1$. The figures show that increasing t_2 leads to a drop in the DOS of QD1 while the DOS in QD2 is increased. In addition, the single peak in the first dot transforms into a three-peak due to the Majorana interference with the second dot. In **??** we also observe that the reason between the zero up-down DOS $\left(\frac{\rho_\uparrow(0)}{\rho_\uparrow(0)}\right)$ smoothly scales up to 2 in QD2. At $t_2 = 0.02$, when the is completely symmetric, the Majorana signature appears in both quantum dots. Note that the relation $\frac{\rho_\uparrow(0)}{\rho_\uparrow(0)}$ is already close to 2 at $t_2 = 0$. This implies that the second dot "feels" the Majorana even when it is not directly connected to the Majorana mode.

Figure 5.20: Evolution of the DOS in the first QD

Bibliography

[1] A. Yu Kitaev. Unpaired Majorana fermions in quantum wires. *Phys.-Usp.*, 44(10S):131, 2001. ISSN 1063-7869. doi: 10.1070/1063-7869/44/10S/S29. URL http://stacks.iop.org/1063-7869/44/i=10S/a=S29. 1

[2] Jason Alicea. Majorana fermions in a tunable semiconductor device. *Phys. Rev. B*, 81 (12):125318, March 2010. doi: 10.1103/PhysRevB.81.125318. URL https://link.aps.org/doi/10.1103/PhysRevB.81.125318. 1

[3] Jason Alicea. New directions in the pursuit of Majorana fermions in solid state systems. *Rep. Prog. Phys.*, 75(7):076501, 2012. ISSN 0034-4885. doi: 10.1088/0034-4885/75/7/076501. URL http://stacks.iop.org/0034-4885/75/i=7/a=076501. 1

[4] Dong E. Liu and Harold U. Baranger. Detecting a majorana-fermion zero mode using a quantum dot. 84(20). ISSN 1098-0121, 1550-235X. doi: 10.1103/PhysRevB.84.201308. URL http://arxiv.org/abs/1107.4338. 1, 5.1.2

[5] Minchul Lee, Jong Soo Lim, and Rosa Lopez. Kondo effect in a quantum dot side-coupled to a topological superconductor. 87(24):241402. doi: 10.1103/PhysRevB.87.241402. URL https://link.aps.org/doi/10.1103/PhysRevB.87.241402. 1

[6] E. Vernek, P. H. Penteado, A. C. Seridonio, and J. C. Egues. Subtle leakage of a majorana mode into a quantum dot. 89(16):165314. doi: 10.1103/PhysRevB.89.165314. URL https://link.aps.org/doi/10.1103/PhysRevB.89.165314. 1

[7] M. T. Deng, S. Vaitiekenas, E. B. Hansen, J. Danon, M. Leijnse, K. Flensberg, J. Nygard, P. Krogstrup, and C. M. Marcus. Majorana bound state in a coupled quantum-dot hybrid-nanowire system. 354(6319):1557–1562. ISSN 0036-8075, 1095-9203. doi: 10.1126/science.aaf3961. URL http://science.sciencemag.org/content/354/6319/1557. 1

[8] David A. Ruiz-Tijerina, E. Vernek, Luis G. G. V. Dias da Silva, and J. C. Egues. Interaction effects on a majorana zero mode leaking into a quantum dot. 91(11):115435. doi: 10.1103/PhysRevB.91.115435. URL https://link.aps.org/doi/10.1103/PhysRevB.91.115435. 1

[9] Alexander W. Holleitner, Robert H. Blick, Andreas K. HÃŒttel, Karl Eberl, and JÃ¶rg P. Kotthaus. Probing and Controlling the Bonds of an Artificial Molecule. *Science*, 297 (5578):70–72, July 2002. ISSN 0036-8075, 1095-9203. doi: 10.1126/science.1071215. URL http://science.sciencemag.org/content/297/5578/70. 3.1

[10] Dieter Bimberg, Marius Grundmann, and Nikolai N. Ledentsov. *Quantum Dot Heterostructures*. Wiley, Chichester, Eng.; New York, 1 edition, March 1999. ISBN 978-0-471-97388-1. 3.1, 3.1

[11] Michael Sindel. *Numerical Renormalization Group studies of Quantum Impurity Models in the Strong Coupling Limit*. Text.PhDThesis, Ludwig-Maximilians-UniversitÃt MÃŒnchen, January 2005. URL https://edoc.ub.uni-muenchen.de/3115/. 3.1, 3.3, 3.2, 3.4, 3.3, 4.2

[12] P. W. Anderson. Localized Magnetic States in Metals. *Physical Review*, 124(1):41–53, October 1961. doi: 10.1103/PhysRev.124.41. URL https://link.aps.org/doi/10.1103/PhysRev.124.41. 3.2

[13] Alexander Cyril Hewson. *The Kondo Problem to Heavy Fermions*. Cambridge University Press, April 1997. ISBN 978-0-521-59947-4. Google-Books-ID: fPzgHneNFDAC. 3.3, 3.3

[14] W.J. de Haas, J. de Boer, and G.J. van dÃ«n Berg. The electrical resistance of gold, copper and lead at low temperatures. *Physica*, 1(7):1115 – 1124, 1934. ISSN 0031-8914. doi: https://doi.org/10.1016/S0031-8914(34)80310-2. URL http://www.sciencedirect.com/science/article/pii/S0031891434803102. 3.4

[15] Daniel A Spielman. Algorithms, graph theory, and linear equations in laplacian matrices. In *Proceedings of the International Congress of Mathematicians*, volume 4, pages 2698–2722, 2010. URL http://www.mathunion.org/ICM/ICM2010.4/Main/icm2010.4.2698.2722.pdf. 4.1.1, 4.1.1

[16] Ralf Bulla, Theo A. Costi, and Thomas Pruschke. Numerical renormalization group method for quantum impurity systems. *Reviews of Modern Physics*, 80(2):395–450, April 2008. doi: 10.1103/RevModPhys.80.395. URL https://link.aps.org/doi/10.1103/RevModPhys.80.395. 4.2, 4.2

[17] Kenneth G. Wilson. The renormalization group: Critical phenomena and the Kondo problem. *Reviews of Modern Physics*, 47(4):773–840, October 1975. doi: 10.1103/RevModPhys.47.773. URL https://link.aps.org/doi/10.1103/RevModPhys.47.773. 4.2

[18] H. R. Krishna-murthy, J. W. Wilkins, and K. G. Wilson. Renormalization-group approach to the Anderson model of dilute magnetic alloys. 1. Static properties for the symmetric case. *Phys.Rev.*, B21:1003–1043, 1980. doi: 10.1103/PhysRevB.21.1003. 4.2, 4.2, 4.2

[19] T. A. Costi, A. C. Hewson, and V. Zlatic. Transport coefficients of the Anderson model via the numerical renormalization group. *Journal of Physics: Condensed Matter*, 6(13):2519, 1994. ISSN 0953-8984. doi: 10.1088/0953-8984/6/13/013. URL http://stacks.iop.org/0953-8984/6/i=13/a=013. 4.2.1

[20] Walter Hofstetter. Generalized Numerical Renormalization Group for Dynamical Quantities. *Physical Review Letters*, 85(7):1508–1511, August 2000. doi: 10.1103/PhysRevLett.85.1508. URL https://link.aps.org/doi/10.1103/PhysRevLett.85.1508. 4.2.1

[21] Maissam Barkeshli and Jay D. Sau. Physical Architecture for a Universal Topological Quantum Computer based on a Network of Majorana Nanowires. *arXiv:1509.07135 [cond-mat, physics:quant-ph]*, September 2015. URL http://arxiv.org/abs/1509.07135. arXiv: 1509.07135. 5

[22] Torsten Karzig, Christina Knapp, Roman M. Lutchyn, Parsa Bonderson, Matthew B. Hastings, Chetan Nayak, Jason Alicea, Karsten Flensberg, Stephan Plugge, Yuval Oreg, Charles M. Marcus, and Michael H. Freedman. Scalable designs for quasiparticle-poisoning-protected topological quantum computation with Majorana zero modes. *Physical Review B*, 95(23):235305, June 2017. doi: 10.1103/PhysRevB.95.235305. URL https://link.aps.org/doi/10.1103/PhysRevB.95.235305. 5

[23] M. A. Ruderman and C. Kittel. Indirect Exchange Coupling of Nuclear Magnetic Moments by Conduction Electrons. *Physical Review*, 96(1):99–102, October 1954. doi: 10.1103/PhysRev.96.99. URL https://link.aps.org/doi/10.1103/PhysRev.96.99. B

[24] Kei Yosida. Magnetic Properties of Cu-Mn Alloys. *Physical Review*, 106(5):893–898, June 1957. doi: 10.1103/PhysRev.106.893. URL https://link.aps.org/doi/10.1103/PhysRev.106.893. B

Appendix A

Appendix

A.1 Proof of the Graph Method for Transport Equations.

Appendix B

Three peak appearance in the Double Quantum Dot model.

The DQD model is characterized by the formation of a new state that entangles the two Quantum dots through the leads. This produces an anti-ferromagnetic interaction between the QDs, commonly known as Ruderman-Kittel-Kasuya-Yosida (RKKY) interaction [23, 24]. As consequense, two satelite peaks will emerge in the Density of States.

To explain this phenomenon we will take a symmetric version of Hamiltonian (5.1) with $2e_i = U_i = U$, $t_i = t$ and $t_{dots} = 0$ for $i \in \{1,2\}$.

$$H = \sum_{i,k,\sigma} \frac{U_i}{2}(d^\dagger_{i\sigma}d_{i\sigma} - 1)^2 + t(d_{+,\downarrow} + d^\dagger_{+,\downarrow})\gamma_1 + \Gamma_i(d^\dagger_{i\sigma}c_{k\sigma} + c^\dagger_{k\sigma}d_{i\sigma}). \tag{B.1}$$

The symmetry of the previous Hamiltonian is suitable to apply a base change of the form

$$d_{+,\sigma} = \frac{1}{\sqrt{2}}(d_{1\sigma} + d_{2\sigma}) \ , \ d_{-,\sigma} = \frac{1}{\sqrt{2}}(d_{1\sigma} - d_{2\sigma}).$$

These new operators satisfy the fermionic anti-commutation relations

$$\{d_{\pm,\sigma}, d^\dagger_{\pm,\sigma}\} = 1, \{d_{\pm,\sigma}, d^\dagger_{\mp,\sigma}\} = 0,$$

so that the may be considered as fermion operators. All lineal terms in (B.1) are trivially adapted to the new base. The repulsion potential

$$\sum_i (\sum_\sigma d^\dagger_{i\sigma}d_{i\sigma} - 1)^2 = (\sum_\sigma d^\dagger_{1\sigma}d_{1\sigma} - 1)^2 + (\sum_\sigma d^\dagger_{2\sigma}d_{2\sigma} - 1)^2.$$

gives rise to a non-trivial interaction between the new states. To find this interaction we define the particle number operator

$$\hat{n}_{i,\sigma} := d^\dagger_{i,\sigma}d_{i,\sigma}.$$

So that

$$\hat{n}_{1,\sigma} = \frac{1}{2}\left(\hat{n}_{+,\sigma} + \hat{n}_{-,\sigma} + d^\dagger_{+,\sigma}d_{-,\sigma} + d^\dagger_{-,\sigma}d_{+,\sigma}\right) = \frac{1}{2}\left(\hat{N}_\sigma + \hat{E}_\sigma\right),$$

with $\hat{N} = \hat{n}_{+,\sigma} + \hat{n}_{-,\sigma}$ and $\hat{E}_\sigma = d^\dagger_{+,\sigma}d_{-,\sigma} + d^\dagger_{-,\sigma}d_{+,\sigma}$. Similarly

$$\hat{n}_{2,\sigma} = \frac{1}{2}\left(\hat{N}_\sigma - \hat{E}_\sigma\right).$$

Hence

$$\sum_i (\sum_\sigma d^\dagger_{i\sigma} d_{i\sigma} - 1)^2 = \left(\frac{\hat{N}+\hat{E}}{2} - 1\right)^2 + \left(\frac{\hat{N}-\hat{E}}{2} - 1\right)^2 = \frac{\left(\hat{N}-2\right)^2 - \hat{E}^2}{2},$$

with $\hat{N} = \sum_\sigma \hat{N}_\sigma$, $\hat{E} = \sum_\sigma \hat{E}_\sigma$. Note that opeator $\hat{N}$ represents the total occupation number inside both dots. If this occupation is different than 2 there is an imbalance between particles and dots that is punished by this term. The term E^2 is much more interesting since this one is the responsible for the emergence of satellite peaks in the DOS. To understand what it makes it is simple to observe its results when applied to a based ordered by $|+,-\rangle$.

$$\hat{E}^2|\uparrow,0\rangle = \hat{E}|0,\uparrow\rangle = |\uparrow,0\rangle$$

$$\hat{E}^2|\uparrow,\downarrow\rangle = \hat{E}\left(|0,\uparrow\downarrow\rangle + |\uparrow\downarrow,0\rangle\right) = 2|\uparrow,\downarrow\rangle - 2|\downarrow,\uparrow\rangle$$

The new Hamiltonian

$$H = \sum_\sigma \frac{U}{4}\left(\left(\hat{N}-2\right)^2 - \hat{E}^2\right) + \frac{t}{\sqrt{2}}(d_{+,\downarrow} + d^\dagger_{+,\downarrow})\gamma_1 + \frac{\Gamma}{\sqrt{2}}\sum_k (d^\dagger_{+,\sigma} c_{k\sigma} + c^\dagger_{k\sigma} d_{+,\sigma}) \tag{B.2}$$

is represented in **??**

We can explain this three-peak as the result of a new strong coupling interaction characterized by the spin exchange between both dots.

In addition, the spin-up DOS at the Fermi energy grows faster than the spin-down DOS, breaking the initial spin-symmetry when $t_1 = t_2 = 0$. At $t_1 = t_2 = 0.02D$ the spin-up DOS at the fermi energy doubles the spin-down DOS which implies that the Majorana signature is present in both dots. Indeed **??** shows that the relation $\frac{\rho_\uparrow(0)}{\rho_\uparrow(0)}$ increases continuously from 1 to 2. Note that the Majorana is completely attached when the coupling t_1 reaches the order of $0.01D$.

B.1 Initial DQD-Majorana Hamiltonian.

$H_{N_\uparrow=0,P_\downarrow=-1}$:

$$\begin{array}{c} |\downarrow,\downarrow,\downarrow\rangle \rightarrow \\ |0,0,\downarrow\rangle \rightarrow \\ |0,\downarrow,0\rangle \rightarrow \\ |\downarrow,0,0\rangle \rightarrow \end{array} \begin{bmatrix} \varepsilon_d^+ + \frac{U^+}{2} - 2h + \varepsilon_m & 0 & -\tilde{t}_{+1} & \tilde{t}_{+2} \\ 0 & \frac{U^+}{2} + \varepsilon_m & \tilde{t}^*_{-2} & \tilde{t}^*_{-1} \\ -\tilde{t}^*_{+1} & \tilde{t}_{-2} & \varepsilon_{d_2} + \frac{U^+}{2} - h - \varepsilon_m & t \\ \tilde{t}^*_{+2} & \tilde{t}_{-1} & t^* & \varepsilon_{d_1} + \frac{U^+}{2} - h - \varepsilon_m \end{bmatrix}$$

$H_{N_\uparrow=0,P_\downarrow=1}$:

$$\begin{array}{c} |0,0,0\rangle \to \\ |\downarrow,\downarrow,0\rangle \to \\ |\downarrow,0,\downarrow\rangle \to \\ |0,\downarrow,\downarrow\rangle \to \end{array} \begin{bmatrix} \frac{U^+}{2}-\varepsilon_m & 0 & \tilde{t}_{+1} & \tilde{t}_{+2} \\ 0 & \varepsilon_d^+ + \frac{U^+}{2} - 2h - \varepsilon_m & \tilde{t}^*_{-2} & -\tilde{t}^*_{-1} \\ \tilde{t}^*_{+1} & \tilde{t}_{-2} & \varepsilon_{d_1} + \frac{U^+}{2} - h + \varepsilon_m & t \\ \tilde{t}^*_{+2} & -\tilde{t}_{-1} & t^* & \varepsilon_{d_2} + \frac{U^+}{2} - h + \varepsilon_m \end{bmatrix}$$

$H_{N_\uparrow=2,P_\downarrow=-1}$:

$$\begin{array}{c} |\uparrow\downarrow,\uparrow\downarrow,\downarrow\rangle \to \\ |\uparrow,\uparrow,\downarrow\rangle \to \\ |\uparrow,\uparrow\downarrow,0\rangle \to \\ |\uparrow\downarrow,\uparrow,0\rangle \to \end{array} \begin{bmatrix} 2\varepsilon_d^+ + \frac{3U^+}{2} + \varepsilon_m & 0 & \tilde{t}_{+1} & \tilde{t}_{+2} \\ 0 & \varepsilon_d^+ + \frac{U^+}{2} + 2h + \varepsilon_m & \tilde{t}^*_{-2} & -\tilde{t}^*_{-1} \\ \tilde{t}^*_{+1} & \tilde{t}_{-2} & f(d_1,d_2) + h - \varepsilon_m & -t \\ \tilde{t}^*_{+2} & -\tilde{t}_{-1} & -t^* & f(d_2,d_1) + h - \varepsilon_m \end{bmatrix}$$

with $f(d_i,d_j) = \varepsilon_{d_i} + \frac{U_i}{2} + 2\varepsilon_{d_j} + \frac{3U_j}{2}$.
$H_{N_\uparrow=2,P_\downarrow=1}$:

$$\begin{array}{c} |\uparrow,\uparrow,0\rangle \to \\ |\uparrow\downarrow,\uparrow\downarrow,0\rangle \to \\ |\uparrow\downarrow,\uparrow,\downarrow\rangle \to \\ |\uparrow,\uparrow\downarrow,\downarrow\rangle \to \end{array} \begin{bmatrix} \varepsilon_d^+ + \frac{U^+}{2} + 2h - \varepsilon_m & 0 & -\tilde{t}_{+1} & \tilde{t}_{+2} \\ 0 & 2\varepsilon_d^+ + \frac{3U^+}{2} - \varepsilon_m & \tilde{t}^*_{-2} & \tilde{t}^*_{-1} \\ -\tilde{t}^*_{+1} & \tilde{t}_{-2} & f(d_2,d_1) + h + \varepsilon_m & -t \\ \tilde{t}^*_{+2} & \tilde{t}_{-1} & -t^* & f(d_1,d_2) + h + \varepsilon_m \end{bmatrix}$$